MT-CWR-092-013

(2)

Annual Progress Report

SHIELDED METAL ARC WELDING CONSUMABLES FOR ADVANCED HIGH STRENGTH STEELS

(Work performed under Contract N00014-89-J-3170)

S. Liu, G.L. Fredrickson, M.Q. Johnson, and G.R. Edwards

Center for Welding and Joining Research
Colorado School of Mines
Golden, Colorado 80401

February 1992

MT-CWR-092-013

Annual Progress Report

Shielded Metal Arc Welding Consumables for Advanced High Strength Steels

(Work performed under Contract N00014-89-J-3170)

Submitted to:

U.S. Office of Naval Research
Materials Division - Code 1131
800 North Quincy Street
Arlington, Virginia 22217-5000

and

David Taylor Research Center
Fabrication Technology - Code 2815
Annapolis, Maryland 21402-5067

Submitted by:

S. Liu, G. L. Fredrickson, M. Q. Johnson, and G. R. Edwards
Center for Welding and Joining Research
Colorado School of Mines
Golden, Colorado 80401

February 1992

Table of Contents:

Abstract

To achieve the goal of developing adequate shielded metal arc (SMA) welding consumables for advanced high strength steels, the complex relationship between flux coating and base metal must be understood. This report is concerned with the effect of flux ingredients on high strength steel welding. Submerged arc (SA) welding was first used to investigate the performance of 45 experimental flux compositions chosen from the $CaCO_3$-SiO_2-K_2SiO_3-CaF_2-Fe system. Bead-on-plate welds were produced on 3/4 in. (19.1 mm) thick HSLA-100 steel plates using a 1/16 in. (1.59 mm) diameter Airco AX-140 welding wire. A 1.5 kJ/mm (38.1 kJ/in.) linear heat input was maintained for all welds. To evaluate the effect of the experimental fluxes, two empirical basicity indexes were used: the basicity index (B_I) and the Zeke basicity index (B_z). Experimental results showed definite influences of the flux ingredients, both on weld bead morphology and chemical composition of the weld metal. As the basicity of the flux increases, the weld metal oxygen content decreases and the weld metal carbon equivalent (P_{cm}) increases. As weld metal oxygen content decreases, the amount of acicular ferrite and Charpy-V-notch impact toughness of the weld metal are observed to increase. The submerged arc welding results also showed that while B_I can describe satisfactorily the behavior of basic fluxes, B_z is more appropriate for the acidic fluxes.

Using the submerged arc welding data, four fluxes were selected for the extrusion of experimental SMA electrodes. Welding was performed at similar conditions as the submerged arc welds. Slag coverage, weld bead morphology, and weld metal microstructures confirmed the results obtained in submerged arc welding. Diffusible hydrogen content was also low in all SMA welds (from approximately 2 to 8 ml/100g weld metal).

I. Introduction

Utilization of low carbon microalloyed steels with yield strengths greater than 690 MPa (100 ksi) depends on the availability of adequate welding consumables. In the case of shielded metal arc welding, the electrodes must provide shielding for the molten weld pool and protect the transfer of alloying elements across the arc to result in a weld joint that exhibit acceptable strength and toughness. However, the control of weld metal chemical composition for acceptable weld quality requires a fundamental understanding of the interaction of the core wire, flux

coating, and base metal. This investigation has systematically varied the composition of the flux coatings of shielded metal arc electrodes for welding advanced high strength steels. To minimize oxygen and hydrogen pickup in the weld metal, a majority of the flux systems considered were basic in nature. While CaF_2 and $CaCO_3$ were the ingredients in the experimental fluxes that exhibit basic nature, K_2SiO_3 and Na_2SiO_3, two commonly used binders, SiO_2 and iron powder were also added to simulate the flux composition of commercially available basic shielded metal arc electrodes. Each of the flux components was selected to evaluate its effect on slag formation, weld pool refining, and its ability to produce a strong and tough weld deposit.

II. Development to Date

II.1. Submerged arc welding

II.1.1. Experimental Procedure

Forty five quasi-ternary experimental fluxes were prepared from high purity $CaCO_3$, CaF_2, SiO_2, $K_2SiO_3.nH_2O$, and Fe powder. These chemicals, at the right amount and proportion, were thoroughly mixed and dried at 160°C for three to six hours. The baking removed moisture from the flux composition, particularly the moisture associated with the potassium silicate binder ($K_2SiO_3.nH_2O$). The fluxes were then crushed and sized to 14# Tyler mesh (1.7 mm screen aperture) to generate a flux consistency (granularity) adequate for the submerged arc welding process. Following sizing, the fluxes were again baked, and stored in air-tight jars until welding. The Oerlikon OP121TT flux was also used to produce welds for comparison. Through a simple evaporation experiment it was determined that the hydrated potassium silicate binder ($K_2SiO_3.nH_2O$) used in this investigation was 50 wt. pct. potassium silicate (K_2SiO_3) and 50 wt. pct. water (H_2O). The coefficient n in the chemical formula of potassium silicate is approximately equal to 8. Experimental flux composition data are all expressed in terms of the dehydrated form of potassium silicate binder (K_2SiO_3). The chemical composition of the experimental fluxes investigated and their basicity index values are reported in Table I.

Notice that the fluxes have been renamed since the 1991 report (Ref. 1): A1 to A9 (from the 1991 report) are now AA1 to AA9. Similarly, A10 to A18 are AB1 to AB9; B1 to B9 are BA1 to BA9; C1 to C9 are CA1 to CA9; and finally, C10 to C18 are CB1 to CB9.

Table I. Chemical Composition (in wt. pct.) of the experimental fluxes.

Flux ID	$CaCO_3$	CaF_2	K_2SiO_3	SiO_2	Fe	B$_I$*	B$_z$**
AA1	47.1	11.8	17.7	0	23.5	7.1	0.22
AA2	35.3	23.5	17.7	0	23.5	7.9	0.13
AA3	23.5	35.3	17.7	0	23.5	8.6	0.06
AA4	44.4	22.2	11.1	0	22.2	12.5	0.20
AA5	33.3	33.3	11.1	0	22.2	13.6	0.13
AA6	22.2	44.4	11.1	0	22.2	14.7	0.07
AA7	42.1	31.6	5.3	0	21.1	28.5	0.18
AA8	31.6	42.1	5.3	0	21.1	30.7	0.12
AA9	21.1	52.6	5.3	0	21.1	33.0	0.07
AB1	47.1	0	17.7	0	35.3	5.4	0.30
AB2	35.3	11.8	17.7	0	35.3	6.2	0.17
AB3	23.5	23.5	17.7	0	35.3	6.9	0.08
AB4	44.4	11.1	11.1	0	33.3	9.9	0.26
AB5	33.3	22.2	11.1	0	33.3	11.0	0.16
AB6	22.2	33.3	11.1	0	33.3	12.2	0.08
AB7	42.1	21.1	5.3	0	31.6	23.4	0.23
AB8	31.6	31.6	5.3	0	31.6	25.6	0.15
AB9	21.1	42.1	5.3	0	31.6	27.9	0.08
BA1	40.0	10.0	0	30.0	20.0	1.1	-0.47
BA2	30.0	20.0	0	30.0	20.0	1.2	-0.45
BA3	20.0	30.0	0	30.0	20.0	1.4	-0.43
BA4	40.0	20.0	0	20.0	20.0	2.1	-0.18
BA5	30.0	30.0	0	20.0	20.0	2.3	-0.21
BA6	20.0	40.0	0	20.0	20.0	2.6	-0.23
BA7	40.0	30.0	0	10.0	20.0	5.2	0.04
BA8	30.0	40.0	0	10.0	20.0	5.7	-0.17
BA9	20.0	50.0	0	10.0	20.0	6.1	-0.06
CA1	31.6	10.5	5.3	31.6	21.1	0.9	-0.57
CA2	21.1	21.1	5.3	31.6	21.1	1.1	-0.53
CA3	42.1	10.5	5.3	21.1	21.1	1.6	-0.25
CA4	31.6	21.1	5.3	21.1	21.1	1.8	-0.27
CA5	21.1	31.6	5.3	21.1	21.1	2.0	-0.28
CA6	52.6	10.5	5.3	10.5	21.1	3.4	0.11
CA7	42.1	21.1	5.3	10.5	21.1	3.8	0.02
CA8	31.6	31.6	5.3	10.5	21.1	4.2	-0.04
CA9	21.1	42.1	5.3	10.5	21.1	4.5	-0.08
CB1	22.2	11.1	11.1	33.3	22.2	0.8	-0.68
CB2	11.1	22.2	11.1	33.3	22.2	0.9	-0.62

Flux ID	$CaCO_3$	CaF_2	K_2SiO_3	SiO_2	Fe	B_l*	B_z**
CB3	33.3	11.1	11.1	22.2	22.2	1.4	-0.36
CB4	22.2	22.2	11.1	22.2	22.2	1.6	-0.36
CB5	11.1	33.3	11.1	22.2	22.2	1.8	-0.35
CB6	44.4	11.1	11.1	11.1	22.2	2.8	0.00
CB7	33.3	22.2	11.1	11.1	22.2	3.1	-0.07
CB8	22.2	33.3	11.1	11.1	22.2	3.4	-0.12
CB9	11.1	44.4	11.1	11.1	22.2	3.7	-0.15

$$*B_l = \frac{CaO + CaF_2 + K2O}{SiO_2}$$

$$**B_z = \frac{nO^{2-}}{(nO^{2-} > 0) + nX}$$ (*See Section II.1.2.2 for explanation.*)

The as-received HSLA-100 steel plates were cut into strips approximately 5 in. (127 mm) wide and 8 in. (203 mm) long. The weld axis was perpendicular to the direction of hot rolling. The steel coupons received blanchard grinding on both faces and were degreased prior to welding.

The submerged arc welding process was used to produce all the experimental welds. The welding parameters were: travel speed of 15 ipm (6.5 mm/s), welding current of 320 A (wire feed rate of 225 ipm), welding voltage of 30 V, and a contact tip-to-work distance of 1 in., which resulted in a linear heat input of approximately 1.5 kJ/mm (38.1 kJ/in.). All welds were bead-on-plate and produced using 0.0625 in. (1.6 mm) diameter Airco AX-140 welding wire. Additional bead-in-groove welds were also produced specifically for Charpy-V-notch testing. The V-grooves were machined 4 mm (0.16 in.) deep with 60° included angle. The chemical compositions of the steel plate and welding wire are given Table II.

Table II. Chemical composition (in wt. pct.) of HSLA-100 steel and Airco AX-140 filler wire for welding high strength steels.

	C	Mn	Si	P	S	Ni	Mo	Cr	Cu	V	Ti
HSLA-100 Steel	0.053	0.78	0.32	0.009	0.002	3.18	0.59	0.51	1.416	0.004	0.004
Airco AX-140 Electrode	0.076	1.55	0.39	0.004	0.002	2.47	0.80	0.73	0.031	0.003	0.016

Each individual weld was examined with respect to bead morphology, hardness, weld metal microstructure, bulk chemical composition, and interstitial elements. Light microscopy was performed on selected weld specimens to establish the trends of various microstructural constituents as a function of the welding flux composition. Microstructural constituents were categorized into five classifications: primary ferrite (PF), acicular ferrite (AF), ferrite with aligned second phase (FS[A]), ferrite with non-aligned second phase (FS[NA]), and martensite-austenite-carbide microconstituents (MAC). In this report, primary ferrite was defined either as ferrite veins or polygonal grains associated with prior austenite grain boundaries. Acicular ferrite (AF) is defined as small non-aligned ferrite laths found within prior austenite grains. Ferrite with aligned second phase is any grouping of two or more parallel laths of ferrite. Ferrite that completely surrounds microphases which are approximately equiaxed and randomly distributed is known as ferrite with non-aligned second phase (FS[NA]). Except for MAC, all microstructural constituents were identified according to the guidelines developed by the International Institute of Welding (IIW) (Ref. 2). The quantitative metallography data of these experimental welds are reported in Table III, which also included the weld made with the Oerlikon flux (weld HOP).

Additional welds were made using low carbon steel plates and processed following the same procedure described above. The low carbon steel weld results were compared with those of the HSLA-100 steel welds.

Three compositions were chosen from each quasi-ternary flux system (AA, AB, BA, CA, and CB) to prepare welds for CVN impact toughness testing. The selection was based on the weld metal microstructures that these fluxes produced. The cross-sectional dimensions of the sub-sized Charpy specimens are 5 mm by 10 mm and the V-notches were 2.0 ± 0.025 mm deep with a notch tip radius of 0.25 ± 0.025 mm, and an inside angle of $45 \pm 1^{\circ}$. The welds made using Oerlikon OP121TT flux (HOP) were also tested. In addition, CVN specimens were machined directly from the HSLA-100 steel plate as control specimens. A total of seventeen sets of specimens were tested at six temperatures: -196, -150, -117, -98, -78, -50, 0, and 100°C. After testing, the percent brittle fracture surface of each specimen was measured using a computerized image analyzer and the percent lateral expansion was determined using a digital caliper. These measurements, together with the impact toughness data, are reported in Table IV.

Table III. Quantitative metallography data of selected experimental welds.

Weld ID	MAC	PF	AF	FS[A]	FS[NA]
HOP	3.4	13.9	45.4	34.3	3.0
HAA1	2.9	13.9	28.7	51.6	2.9
HAA3	7.6	13.7	33.6	40.2	4.9
HAA5	5.3	14.4	30.8	45.0	4.5
HAA7	6.6	11.6	40.6	34.5	6.7
HAA9	2.0	9.8	36.8	42.2	9.2
HAB1	2.0	13.0	33.2	47.2	4.6
HAB3	3.2	12.8	37.1	42.3	4.6
HAB5	4.9	11.0	33.8	43.4	6.9
HAB7	3.7	11.9	27.7	47.2	9.5
HAB9	1.9	11.8	35.8	42.8	7.7
HBA1	3.5	17.5	21.3	54.4	3.3
HBA3	4.2	10.9	31.0	50.3	3.6
HBA5	3.4	8.8	30.2	53.8	3.8
HBA7	2.2	10.3	28.1	55.2	4.2
HBA9	1.4	7.6	46.8	36.7	7.5
HCA1	3.3	15.2	11.5	17.0	53.0
HCA2	1.9	9.9	30.9	39.7	17.6
HCA4	5.9	18.8	12.3	9.0	54.0
HCA7	2.8	12.5	25.0	48.5	11.2
HCA9	4.1	12.4	48.4	29.0	6.1
HCB1	2.6	15.7	30.8	38.8	12.1
HCB2	2.8	12.5	47.3	29.1	8.3
HCB5	4.0	16.4	17.0	15.7	46.9
HCB7	4.0	13.4	34.7	37.4	10.5
HCB9	1.7	12.8	42.8	34.5	8.2

II.1.2. Results and Discussion

II.1.2.1. Effect of Flux Chemical Composition - Viscosity

In this report, a basic slag is defined as an ionic liquid oxide system with free oxygen ions (O^{2-}) present; i.e., all oxygen ion sites associated with ionic acidic oxide species in the slag are filled and an excess of free oxygen ions (O^{2-}) are present to move as separate entities. An acidic slag is an ionic liquid oxide system with virtually no free oxygen ions (O^{2-}) present. This slag would capture any free oxygen

Table IV. Charpy-V-notch impact energies at 60°C for the experimental welds.

Weld ID	Impact Toughness (ft-lb)	Lateral Expansion at Notch (%)	Brittle;e Fracture Surface (%)
HSLA-100	61	42	20
HOP	35	22	30
HAA3	26	14	28
HAA5	25	11	32
HAA7	34	21	29
HAB3	24	13	30
HAB5	22	11	30
HAB7	17	10	34
HBA3	21	13	32
HBA5	22	11	30
HBA7	19	10	39
HCA2	22	10	40
HCA4	19	10	37
HCA7	17	9	31
HCB2	31	17	25
HCB4	26	15	29
HCB7	23	10	30

ions (O^{2-}) present in the system. Since all oxygen ion sites associated with ionic acidic oxide species are not filled, a deficiency of free oxygen ions (O^{2-}) is present. A neutral slag is an ionic liquid oxide system with neither an excess nor a deficiency of oxygen ions (O^{2-}). Examples of the three types of slags are provided below:

$$\text{Basic Slag: } 3CaO + SiO_2 \rightarrow Ca_3SiO_6 \rightarrow 3Ca^{2+} + SiO_4^{4-} + 2O^{2-} \quad (1)$$

$$\text{Neutral Slag: } 2CaO + SiO_2 \rightarrow Ca_2SiO_4 \rightarrow 2Ca^{2+} + SiO_4^{4-} \quad (2)$$

$$\text{Acidic Slag: } CaO + SiO_2 \rightarrow CaSiO_3 \rightarrow Ca^{2+} + SiO_3^{2-} \quad (3)$$

The oxygen ions (O^{2-}) from the calcium oxide (CaO) decrease the extent of polymerization of the silica (SiO_2) tetrahedral structure. The silica (SiO_2) network is completely broken down (i.e., depolymerized) when the mole ratio of calcium oxide (CaO) to silica (SiO_2) reaches 2, which is the neutral slag condition. The silicate ions (SiO_44-) and the calcium ions (Ca^{2+}) have a much greater mobility with respect to each other than do the silicon ions (Si^{4+}) and oxygen ions (O^{2-}) in the

pure silica (SiO_2) slag. Therefore the viscosity of the silica-based slag decreased with calcium oxide (CaO) additions.

Calcium fluoride (CaF_2), like calcium oxide (CaO), also has the ability to depolymerize the silica (SiO_2) tetrahedral structure in a liquid oxide slag system. In comparing calcium oxide (CaO) to calcium fluoride (CaF_2), it is evident that one mole of each has the same potential to depolymerize the silica (SiO_2) tetrahedral network. In practice, however, it is found that calcium fluoride (CaF_2) is somewhat more efficient at fluxing silica (SiO_2) than calcium oxide (CaO). Note the way in which the term "flux" was used; i.e., flux: to add to in small amounts for the purpose of decreasing the viscosity of the slag. Here the solvent (SiO_2) is the slag and the solute (CaO or CaF_2) is the fluxing agent.

For the reasons provided above, both B_I and B_z can be used as an indication of the viscosity and liquidus temperature of the slag. As the B_I value increases, the extent of depolymerization of the acidic oxide components increases, and the viscosity of the slag decreases. Since viscosity can be related to the liquidus temperature of a slag, the liquidus temperature of the slag decreases with increasing B_I value.

II.1.2.2. Effects of Flux Chemical Composition - Chemical Activity

An alternate argument can also be formed suggesting that the B_I value can be used as an indication of the chemical activity of certain species in the slag. For example, as the B_I value increases; the activity of oxygen ions (O^{2-}) decreases (e.g., replacing SiO_2 with CaO decreases the oxygen ion (O^{2-}) content of the slag system); the activity of the metal ions associated with the basic oxides increases (e.g., replacing SiO_2 with CaO increases the calcium ion (Ca^{2+}) content of the slag system); and the activity of the metal ions associated with the acidic oxides decreases (e.g., replacing SiO_2 with CaO decreases the silicon ion (Si^{4+}) content of the slag system).

The B_z value represents the ionic fraction of excess (free) oxygen ions (O^{2-}) in the dissociated molten slag. Therefore, a basic slag has a positive B_z value, a neutral slag has a B_z value of zero, and an acidic slag has a negative B_z value.

The B_z basicity index can be represented by the following mathematical expression (Ref. 3):

$$B_Z = \frac{nO^{2-}}{(nO^{2-} > 0) + nX} \quad (4)$$

where the term nO^{2-} is the number of moles of excess (or, free) oxygen ions (O^{2-}) in 100 grams of dissociated slag. Again, this value is positive for a basic slag, equal to zero for a neutral slag, and negative for an acidic slag. The term nX is the number of moles of all charged ions other than oxygen ions (O^{2-}) in 100 grams of dissociated slag; e.g., calcium ions (Ca^{2+}), fluorine ions (F^{1-}), silicon ions (Si^{4+}), and iron ions (Fe^{2+} or Fe^{3+}). The value of nX is always positive. Furthermore, the term nO^{2-} is added to the term nX in the denominator if and only if the value of nO^{2-} is positive.

The specific form of the mathematical expressions of the two terms nO^{2-} and nX are dependent on the chemical composition of the flux system. Therefore, the expressions must be written such that they properly take into account all of the basic and acidic oxide components of the flux. General forms of the two expressions are as follows:

$$nO^{2-} = \sum mMe_2O + \sum mMeO - (mAl_2O_3 + 2mTiO_2 + 2mSiO_2) \quad (5)$$

$$nX = \sum 2mMe_2O + \sum mMeO + 3(mCaF_2 + mBaF_2) + mSiO_2 + mTiO_2 + 2mAl_2O_3 \quad (6)$$

Where m is the number of moles of the designated oxide species in 100 grams of flux, and Me is any metallic element associated with the basic oxide species. With regards to the flux systems developed for this investigation (i.e., the 45 experimental fluxes), these expressions become:

$$nO^{2-} = mCaO + mK_2O - 2mSiO_2 \quad (7)$$

$$nX = mCaO + 2mK_2O + 3mCaF_2 + mSiO_2 \quad (8)$$

The calculated B_z values of these fluxes ranged from approximately -0.7 to 0.3.

II.1.2.2. Weld Bead Morphology

Even though each of the experimental fluxes contained only five components, analysis of the experimental results showed that it is still impossible to correlate directly the weld properties to any single component of the flux system. Therefore, B_I and B_z are used in this investigation to characterize the behavior of the fluxes and their influence on weld metal properties. Figures 1 and 2 show that as basicity increased, weld bead width also increased. This increase in bead width is reasonable because basic flux components such as CaF_2 and CaO (from the de-

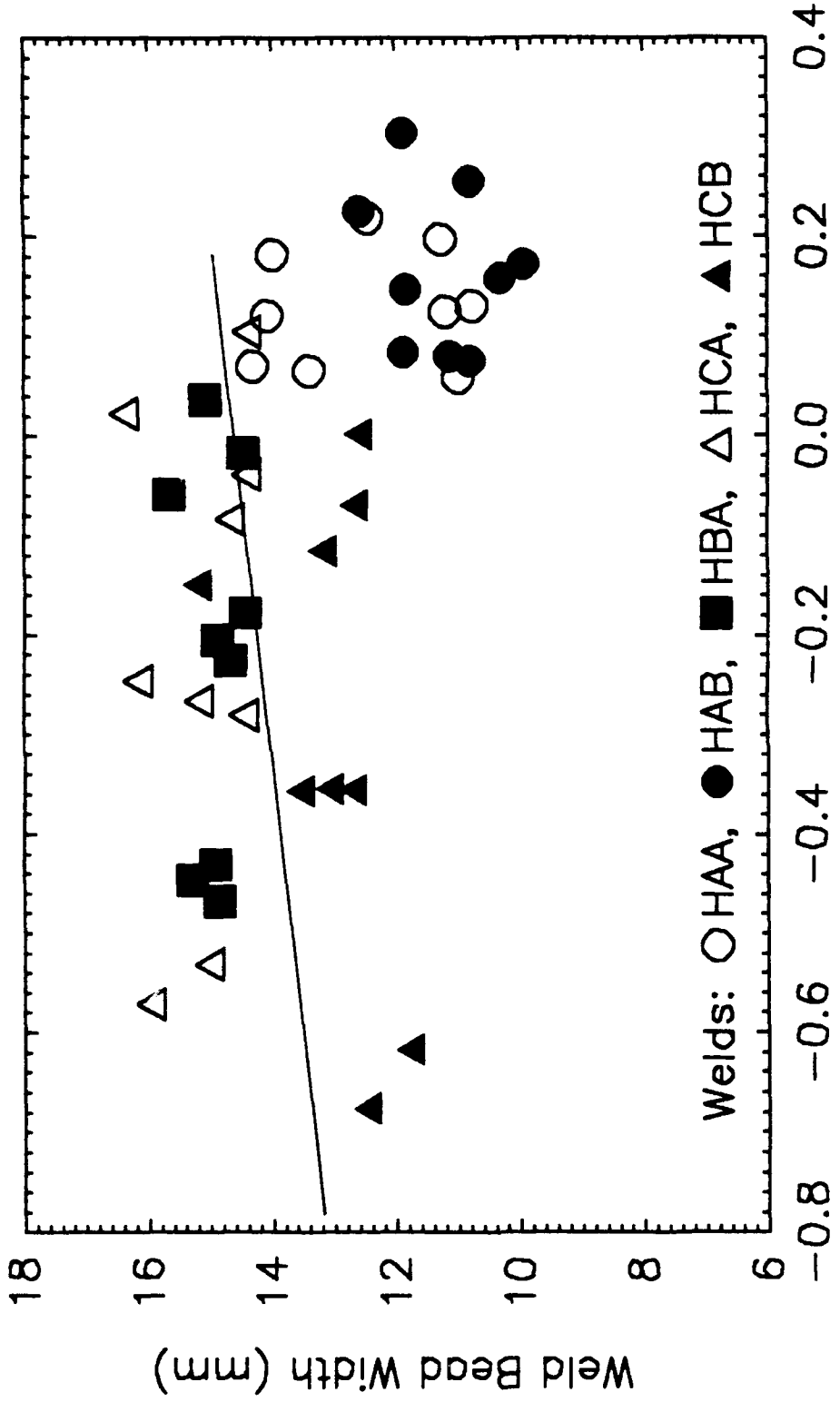

Figure 1. Weld bead width plotted as a function of the Zeke basicity index, B_z.

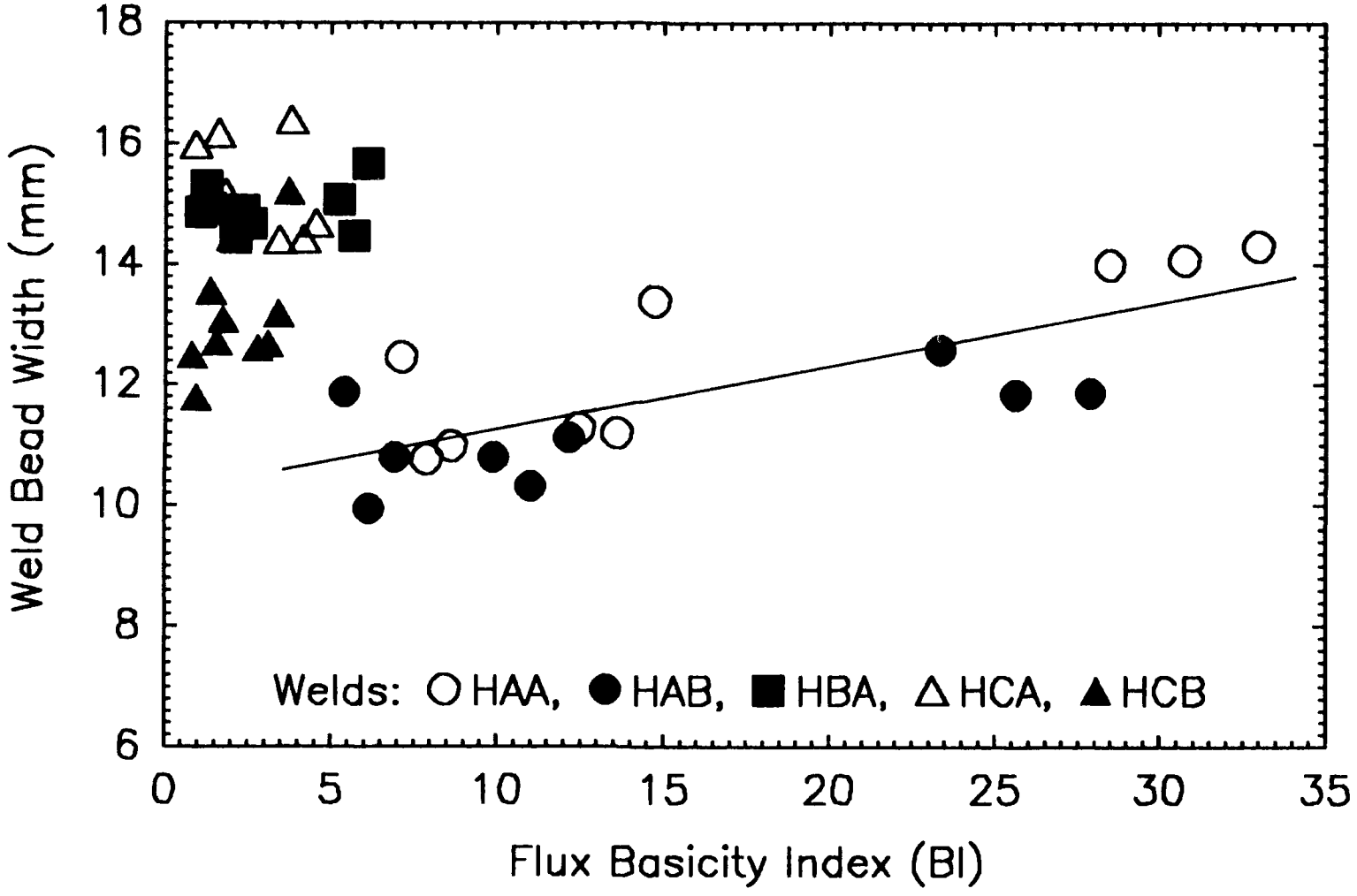

Figure 2. Weld bead width plotted as a function of basicity index, B_I.

composition of $CaCO_3$) are known to decrease the viscosity of a silicate-based slag, which results in a more "runny" slag and a flattened bead. This explanation also agrees with other weld morphology data such as weld bead penetration, which decreased with increasing flux basicity, Figure 3.

However, Figures 2 to 3 also showed a peculiar pattern that when B_I was used to describe the weld bead morphology, the data points that correspond to the welds made using fluxes with high SiO_2 and K_2SiO_3 concentrations were all grouped together. When B_z was used, Figure 1, these same data points were well distributed, showing a clear trend that weld bead width increased with flux basicity. Instead, the data points that correspond to the more basic fluxes with high CaO and CaF_2 are all grouped together. This indicates that, as an indicator of flux viscosity and melting temperature, B_z is capable of describing the behavior of high silicate and silica fluxes. B_I, on the other hand, is more appropriate for more basic fluxes.

Weld HAA7, shown in Figure 4a and 4b, further illustrates the influence of flux composition on weld bead morphology. The regular surface ripple pattern, uniform toe line, and smooth bead-to-plate transition indicate that the molten slag had good flow properties which provided good weld pool shielding and excellent bead surface. This flux contained 31.6 wt.pct. CaF_2, 42.7 wt.pct. $CaCO_3$, 5.3 wt.pct. K_2SiO_3, and 21.1 wt.pct. Fe. the B_I and B_z of this flux were 28.5 and 0.18, respectively.

Weld HAA1, shown in Figure 5a and 5b, is the opposite of the previous example. Rough bead surface, poor bead-to-plate transition, and irregular bead penetration indicate that the flux was too viscous and had a high melting temperature. This flux contained 11.8 wt.pct. CaF_2, 47.1 wt.pct. $CaCO_3$, 17.7 wt.pct. K_2SiO_3, and 23.5 wt.pct. Fe. The the B_I and B_Z of this flux were 7.1 and 0.22, respectively.

II.1.2.3. Weld Metal Chemical Composition

Welding fluxes affect the weld metal chemical composition mainly by the amount of oxygen that they introduce into the weld pool. Depending on the base metal, loss of alloying elements and the formation of oxide inclusions may be expected. Thus, it is extremely important to determine the amount of oxygen originated from each of the major flux components.

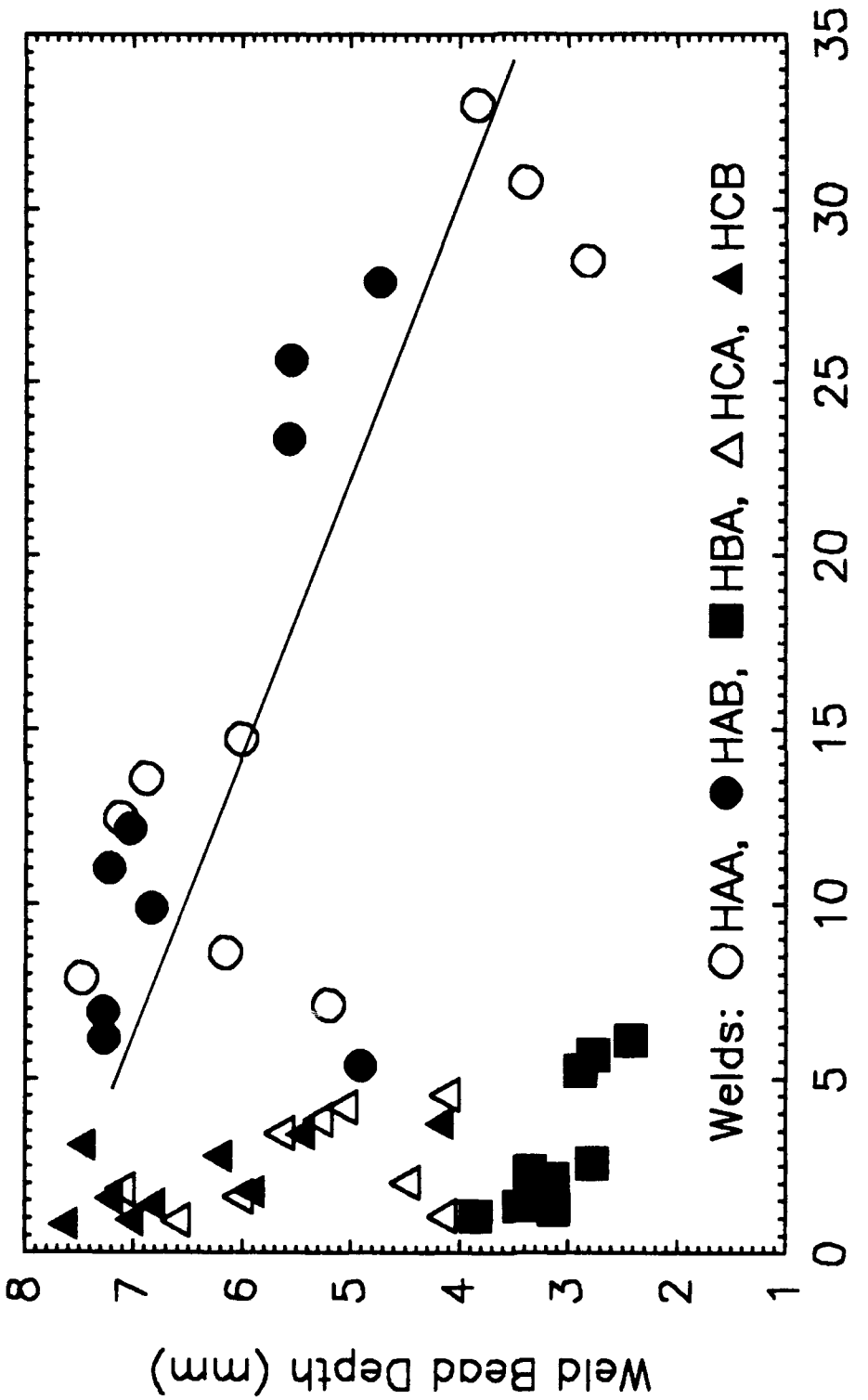

Figure 3. Weld bead depth plotted as a function of basicity index, B_I.

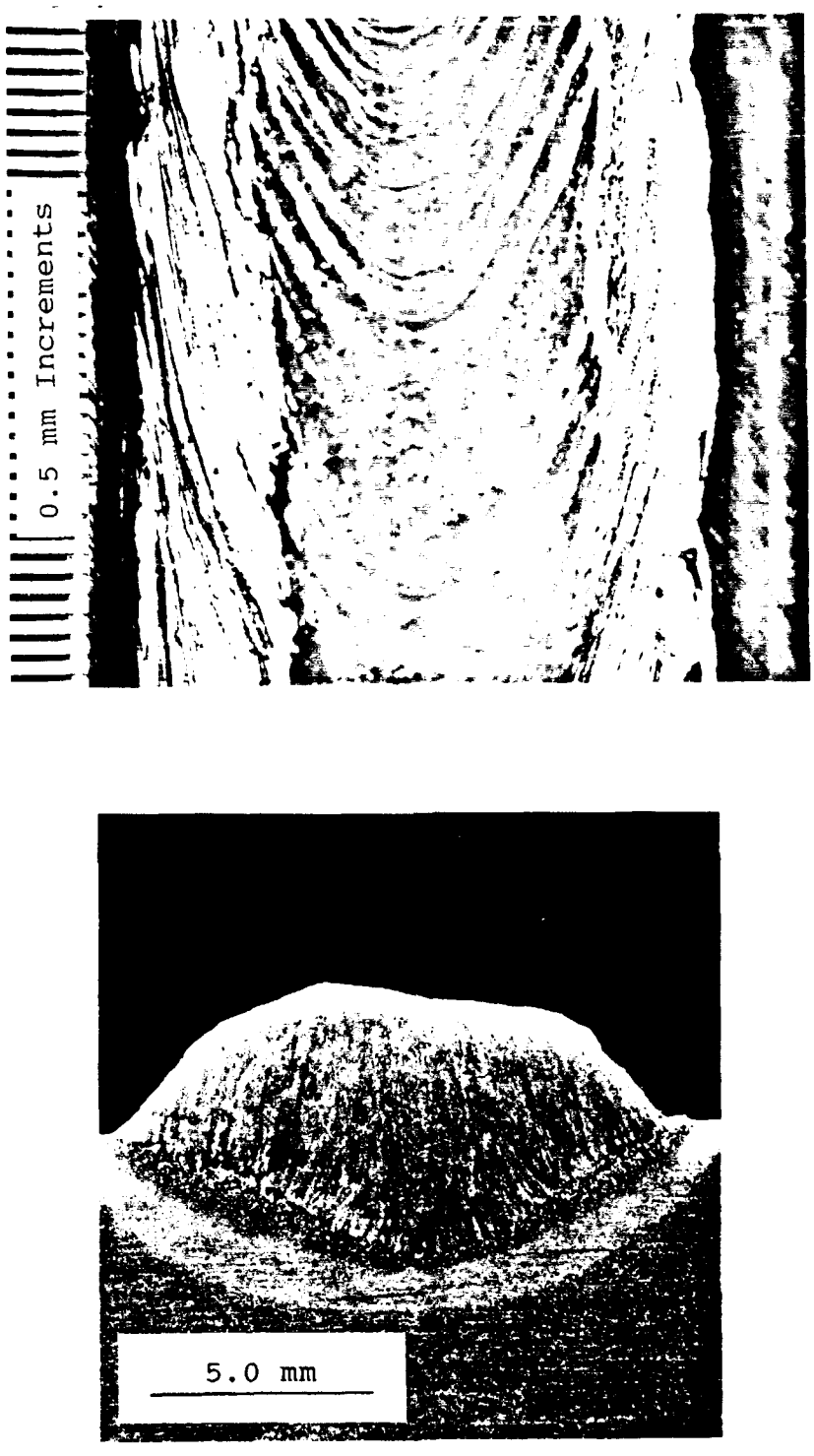

Figure 4. Bead morphology of weld HAA7. (a) Smooth ripple pattern with good bead-to-plate transition; (b) Uniform cross section of the weld bead.

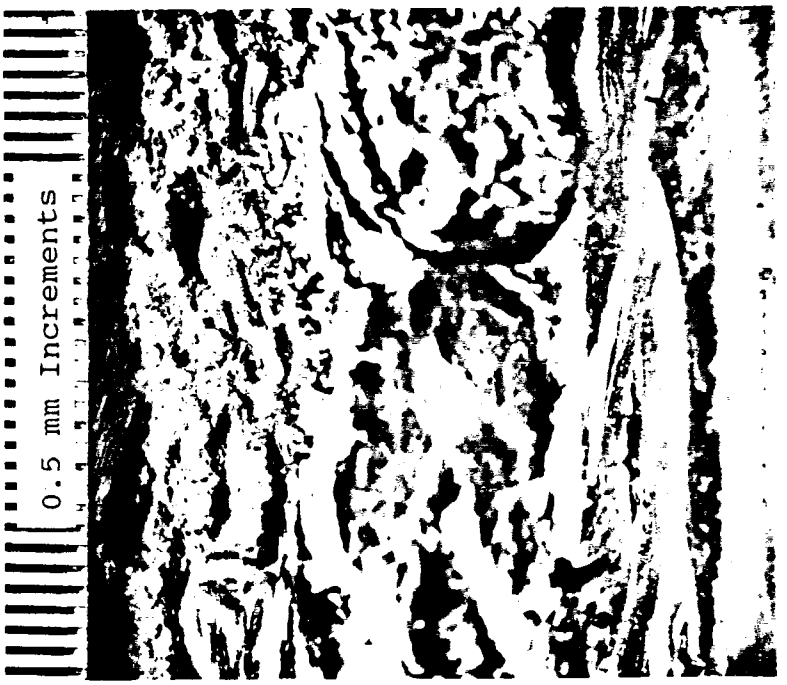

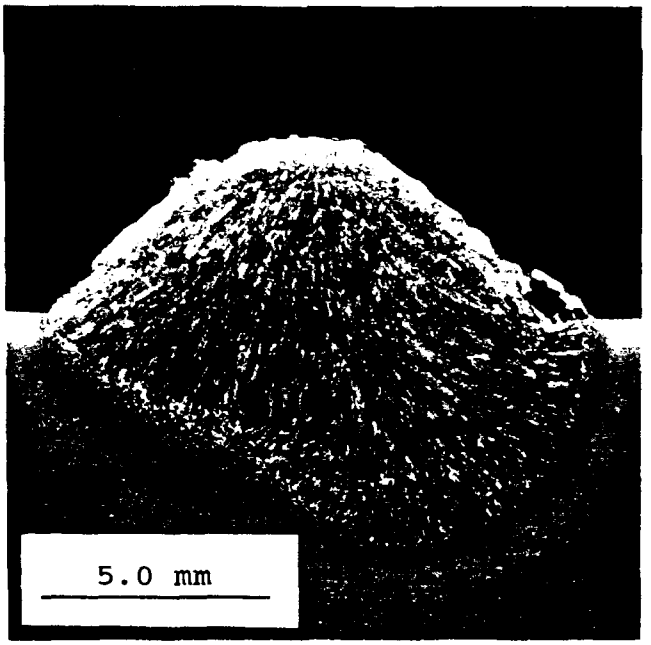

Figure 5. Bead morphology of weld HAA1. (a) Irregular ripple pattern with rough bead-to-plate transition; (b) Non-uniform cross section of the weld bead.

The experimental welds exhibited oxygen contents that varied from 200 to 900 ppm, Figure 6. As the oxygen potential of the flux increased, indicated by the total flux oxygen content, the weld metal oxygen content also increased. Among the five components, CaF_2 contains no oxygen (atomic or ionic) and does not contribute oxygen to the molten metal. The influence of CaF_2 on the final weld metal oxygen content could be attributed to other mechanisms discussed previously. Figure 7 shows that additions of $CaCO_3$ in the flux led to a decrease of weld metal oxygen content. This observation clearly indicates the effect of CO_2, the product of carbonate decomposition in arc shielding. CaO, also a product of carbonate decomposition, is a strong oxide that does not give away its oxygen readily to the weld pool. K_2SiO_3, contrary to what was expected, did not increase the amount of oxygen in weld metal, as shown in Figure 8. Out of the five components, SiO_2 is the only one that promoted an increase in weld metal oxygen content, Figure 9. Being a weak oxide, SiO_2 releases its oxygen with relatively ease and oxidizes the weld pool.

Due to the high oxygen potential of the welding flux with respect to the base metal, it is expected that the base metal composition will play only a minor role in adjusting the final weld pool oxygen content. Welds carried out on both HSLA-100 steel and low carbon steel plates supported the above statement. Oxygen analyses show that the two weld pools were oxidized equally, Figure 10. Despite the larger amount of alloying elements (manganese, nickel, and chromium) in the HSLA-100 steel plate, the low carbon steel (with much leaner composition) experienced similar oxygen pickup.

Figures 11 and 12 show that acidic fluxes provided a larger amount of oxygen in the weld metal. Notice again the effectiveness of B_z in predicting the behavior of acidic fluxes while B_I is more sensitive to basic fluxes. It is, therefore, recommended that the applications of B_z and B_I be limited to acidic and basic fluxes, respectively. However, both basicity indexes failed to describe the effect of K_2SiO_3, that is, decreased oxygen pickup with increasing potassium silicate. It is, therefore, further suggested that the use of basicity index be limited to the description of the physical properties of the welding slag only.

As indicated earlier, oxygen in weld metal could mean alloying element loss. Indeed, weld metal manganese content was observed to decrease from 1.1 to 0.9 wt.pct., Figure 13. Weld HOP was made using the Oerlikon OP121TT flux which contained some MnO and thus, exhibited higher manganese content in the weld

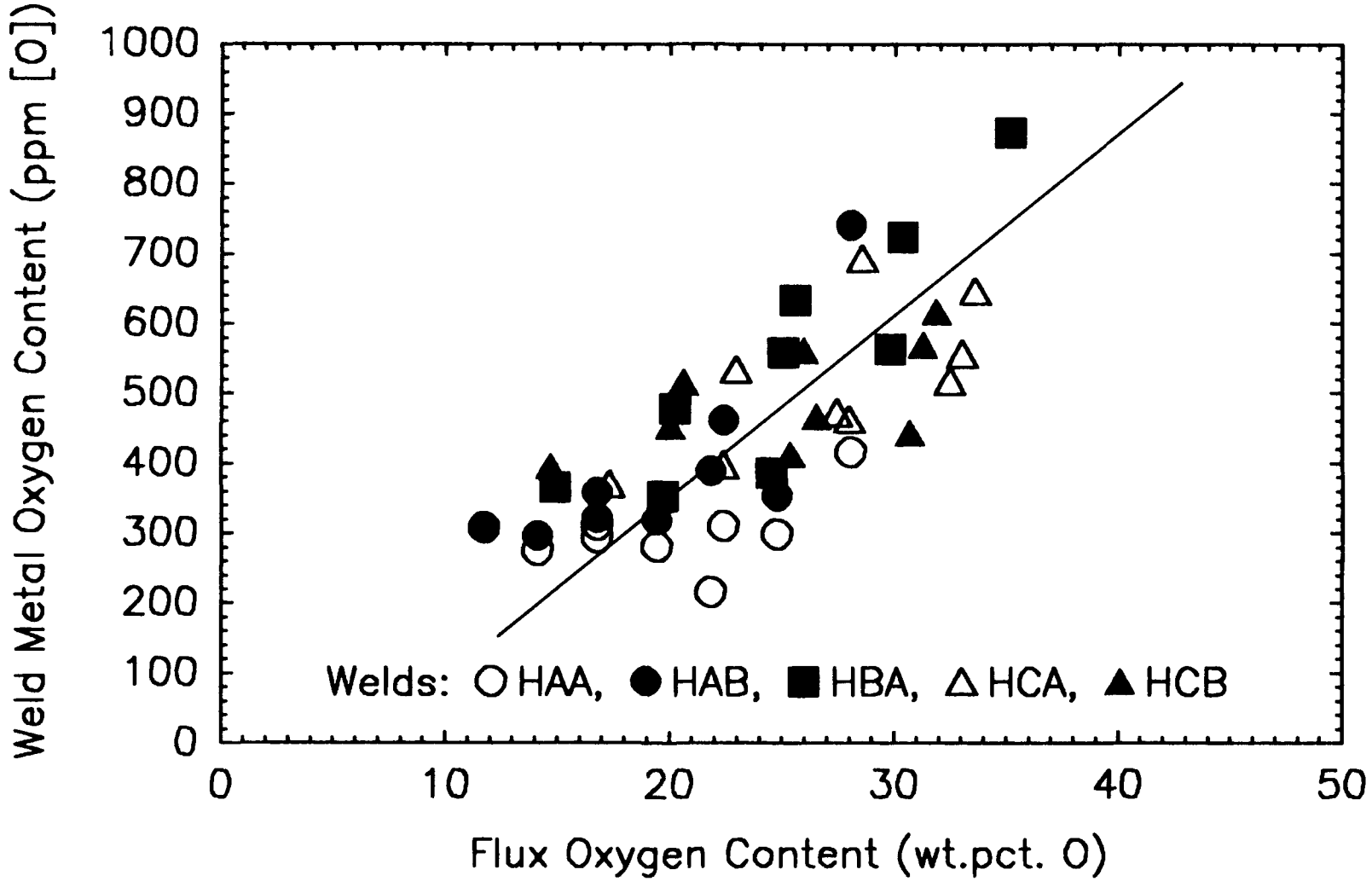

Figure 6. Weld metal oxygen content plotted as a function of the flux oxygen content.

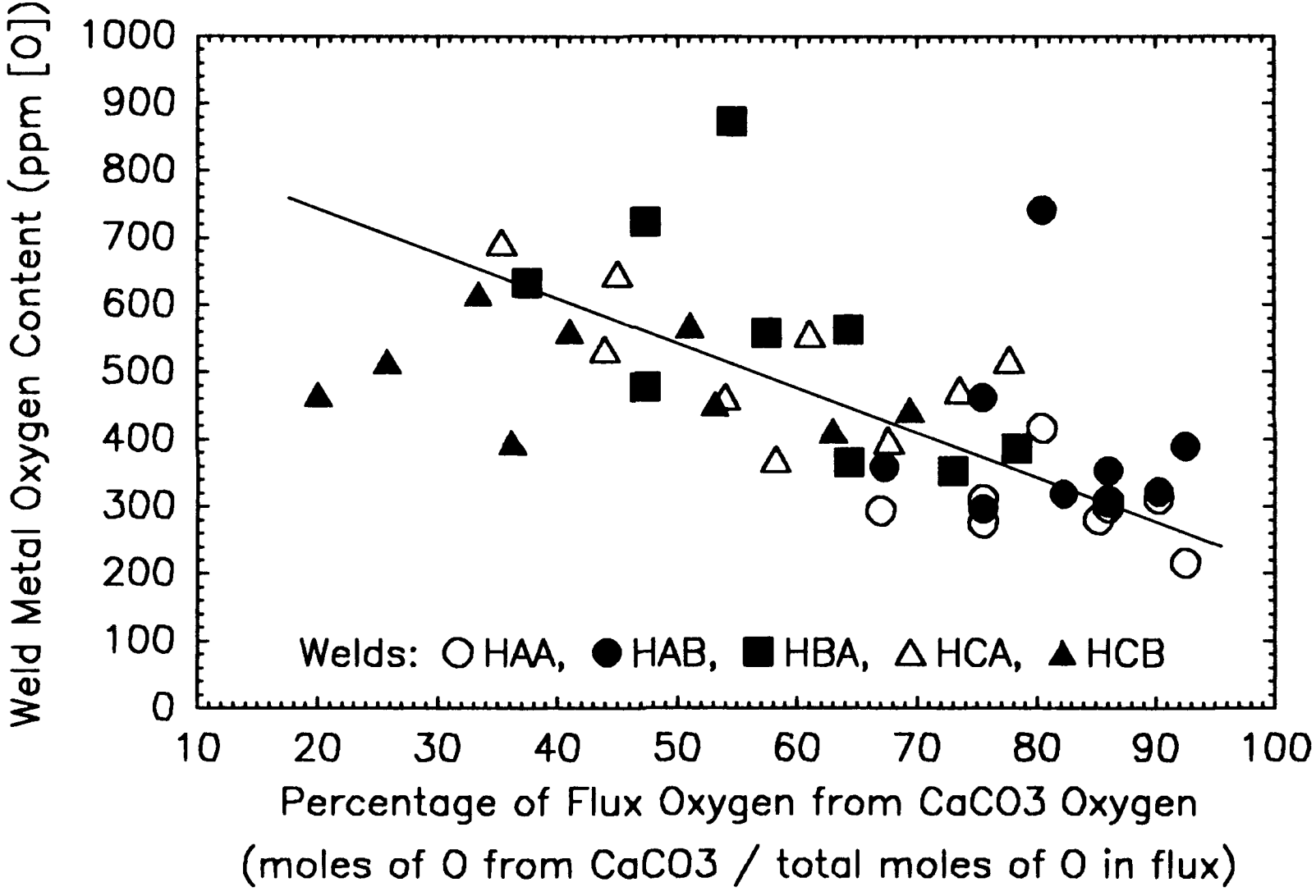

Figure 7. Weld metal oxygen content plotted as a function of the amount of oxygen from $CaCO_3$ in the flux.

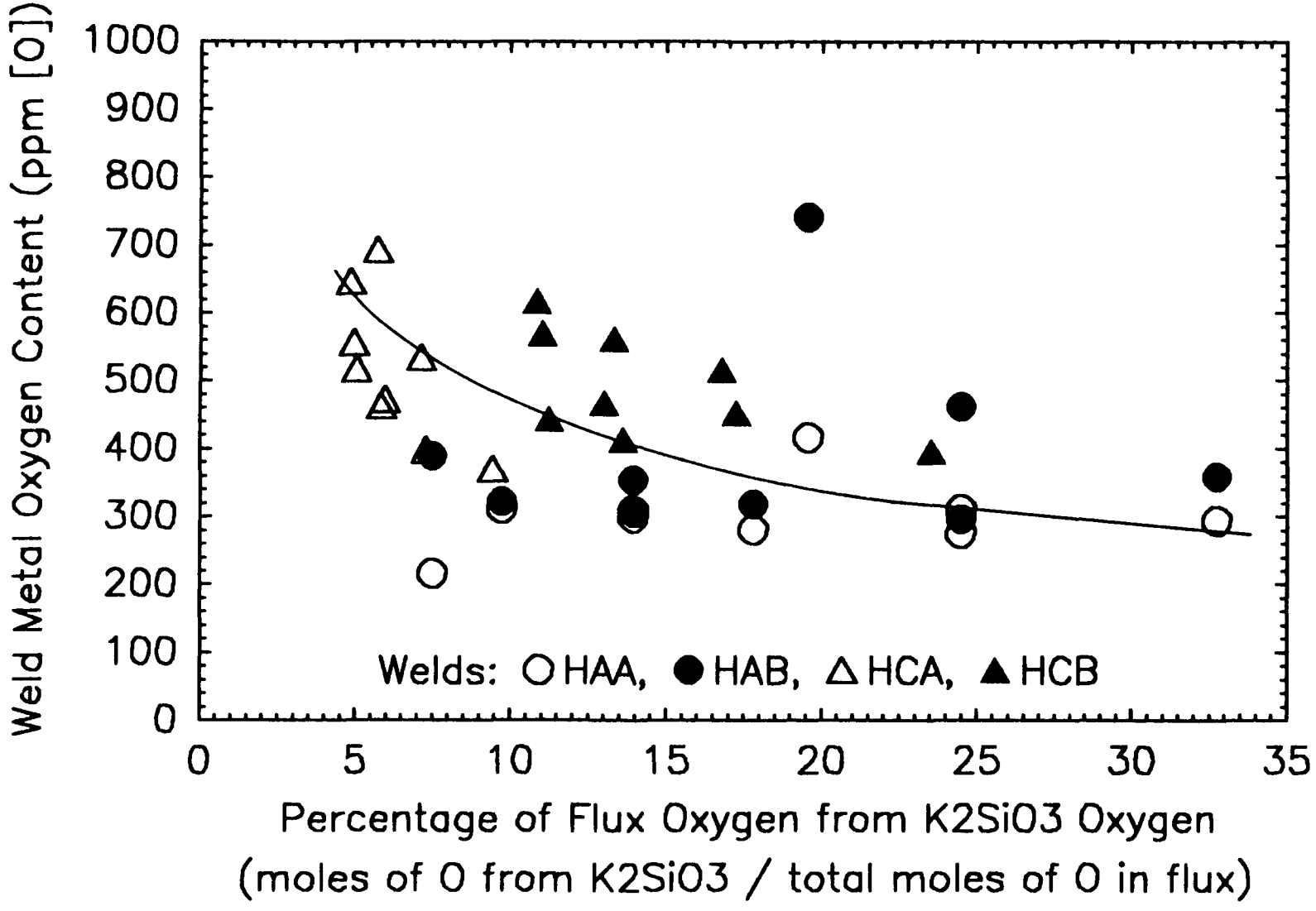

Figure 8. Weld metal oxygen content plotted as a function of the amount of oxygen from K_2SiO_3 in the flux.

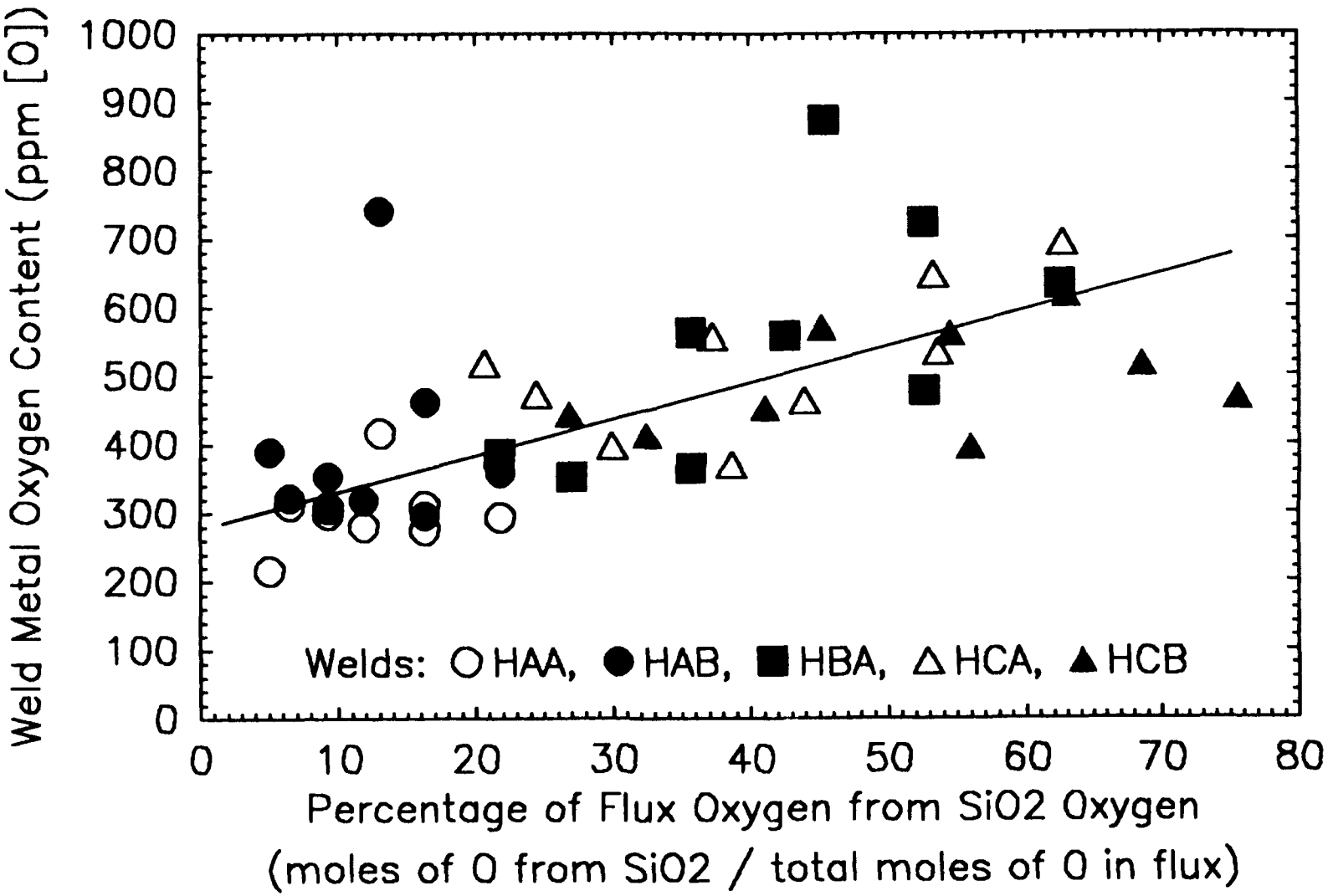

Figure 9. Weld metal oxygen content plotted as a function of the amount of oxygen from SiO_2 in the flux.

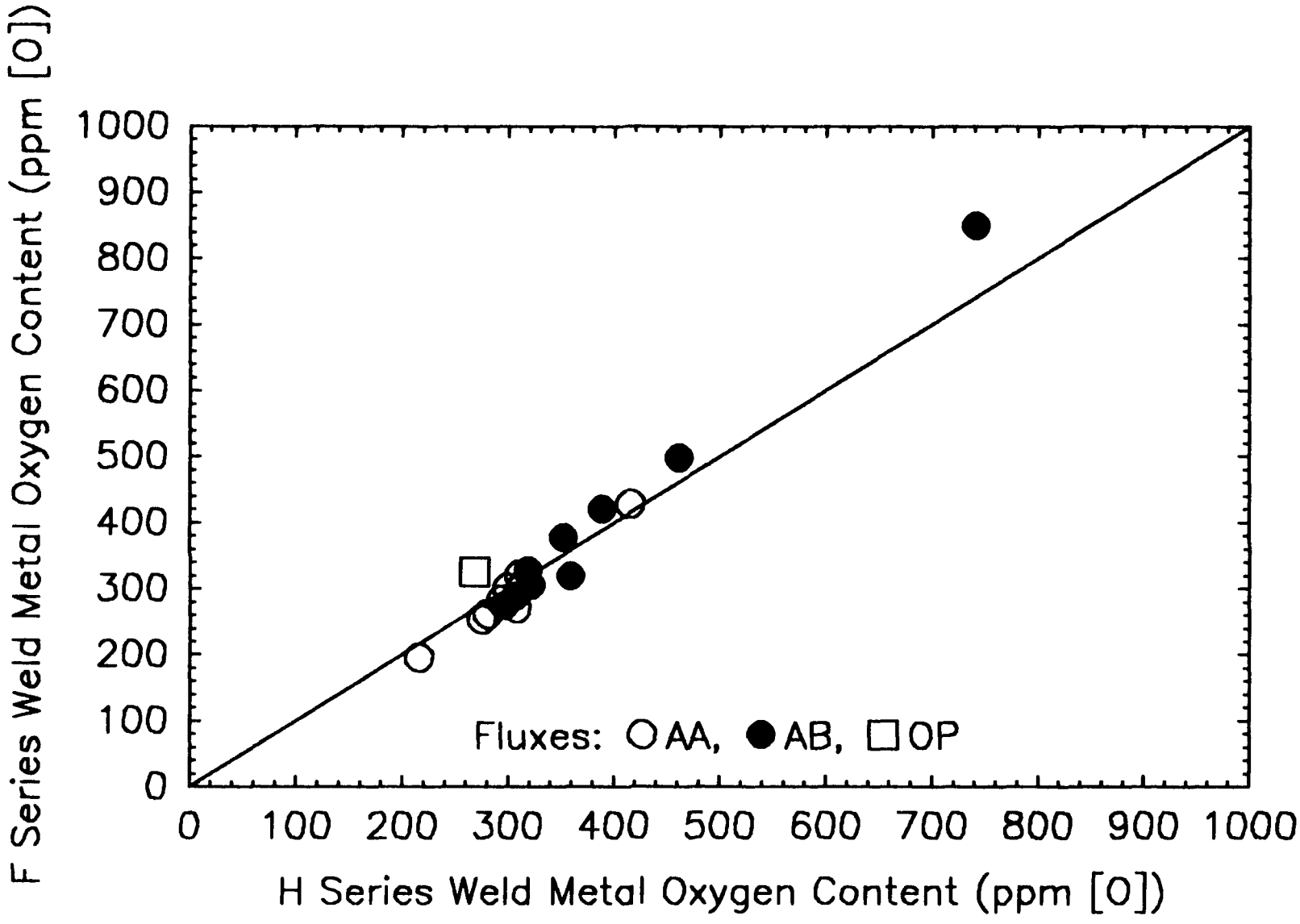

Figure 10. Oxygen content in HSLA-100 steel welds versus oxygen content in AISI 1018 steel welds.

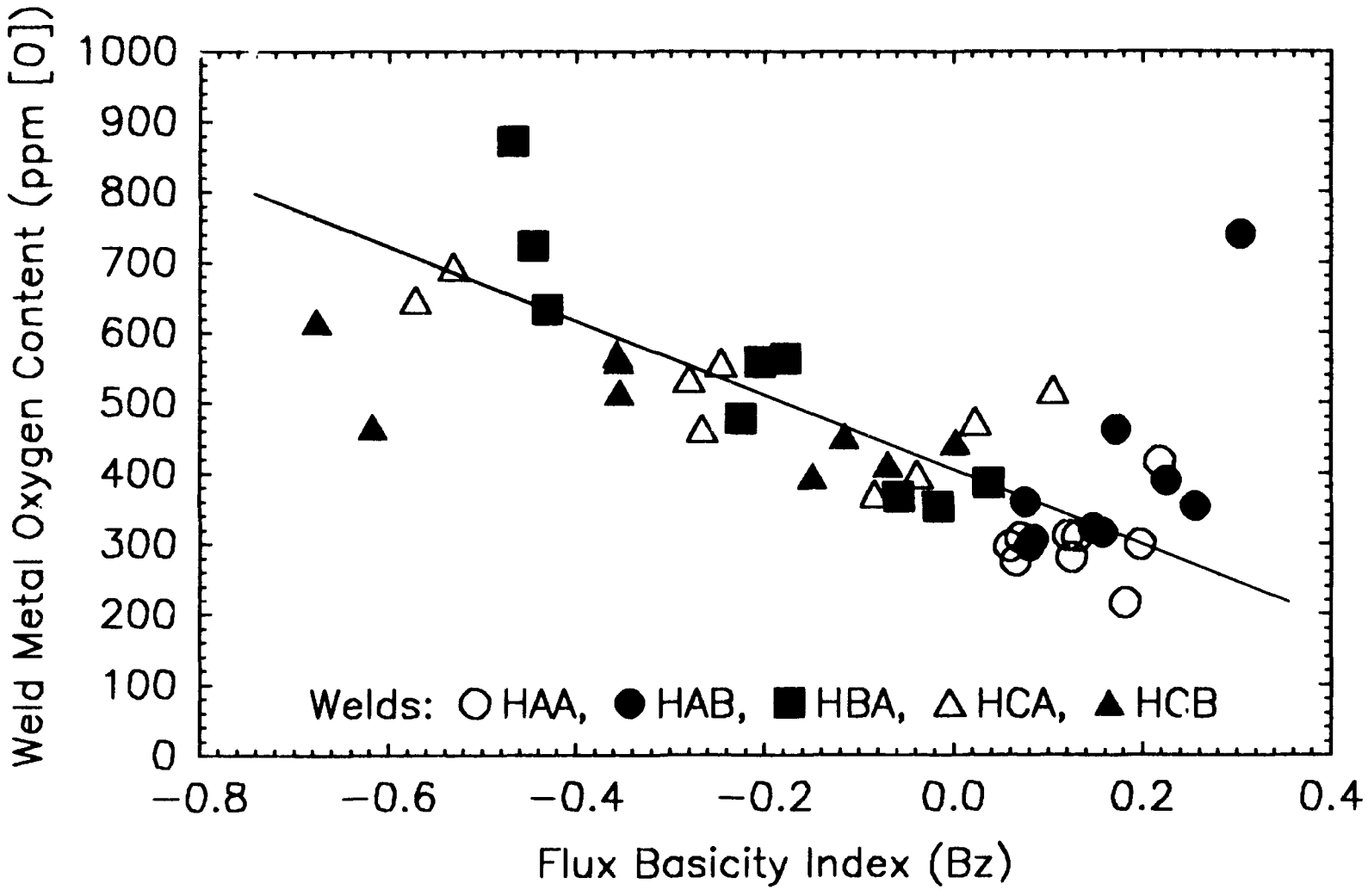

Figure 11. Weld metal oxygen content plotted as a function of the Zeke basicity index, B_z.

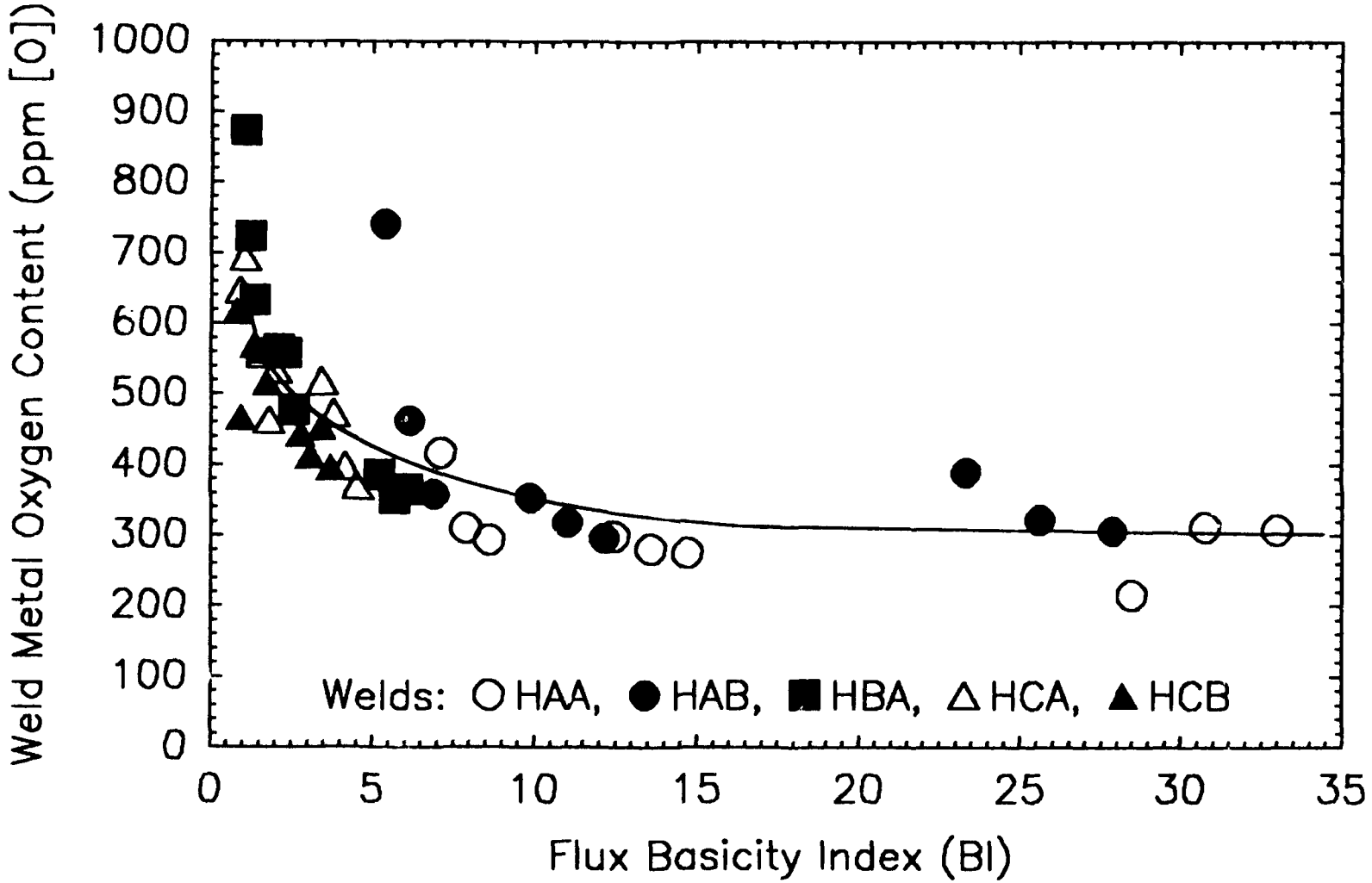

Figure 12. Weld metal oxygen content plotted as a function of basicity index, B_I.

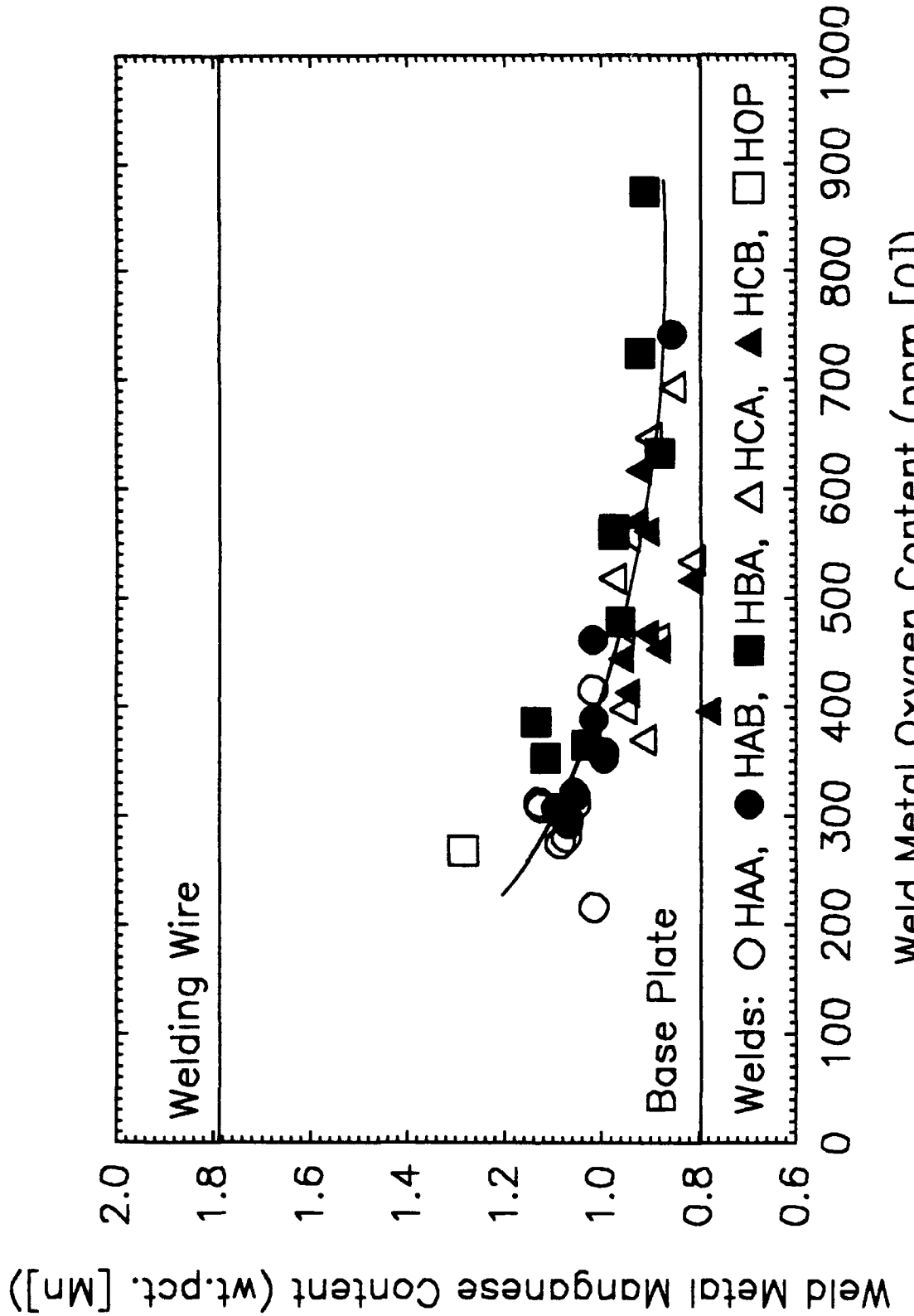

Figure 13. Weld metal manganese content plotted as a function of weld metal oxygen content.

metal than some of the other experimental welds. Besides manganese loss, silicon loss was also observed. However, increasing weld metal silicon content with oxygen, as shown in Figure 14, indicates that inclusions rich in silicon and oxygen were entrapped in the weld metal. No significant changes in carbon, copper, nickel, and chromium were observed. Slight reduction in phosphorus was also observed as shown in Figure 15.

These observations indicate that with the exception of manganese, the flux systems investigated are capable of providing both good shielding for the element transfer across the arc and weld pool recovery. In the case of manganese, adjustments such as ferromanganese additions can be made to the flux formulation such that adequate amounts of manganese be transferred to the weld metal.

With the variation in chemical composition, the chemical hardenability of the weld metal, indicated by P_{cm}, is also affected, as shown in Figure 16. P_{cm} is defined as (Ref. 4):

$$P_{cm} = C + \frac{Si}{30} + \frac{Mn + Cu + Cr}{20} + \frac{Ni}{60} + \frac{Mo + V}{15} + 5B \qquad (7)$$

The observed decrease in P_{cm} with oxygen also hints that the weld metal mechanical properties has changed. Indeed, hardness increased with weld metal P_{cm} and decreased with weld metal oxygen content, Figures 17 and 18.

II.1.2.4. Weld Metal Microstructures

Figures 19 to 26 show the microstructures of some selected experimental welds. As can be seen in Table III, they all contained primary ferrite, acicular ferrite, ferrite with second phase aligned, ferrite with second phase non-aligned, and martensite-austenite-carbide microconstituent. For comparison, micrographs of the base metal and weld HOP are shown in Figures 27 and 28, respectively. While the base metal showed predominately lath martensite and bainite, the microstructure of weld HOP is similar to that of the welds made using the experimental fluxes.

As a result of chemical composition variation, the weld metal microstructure also showed changes. Further analysis showed that the amount of acicular ferrite decreased with weld metal oxygen content, Figure 29. However, the scatter in the experimental data is considerable. A parallel study using low carbon steels resulted in significantly better correlation that the volume fraction of acicular ferrite decreased with weld metal oxygen content, Figure 30. Similarly, Figure 31 in-

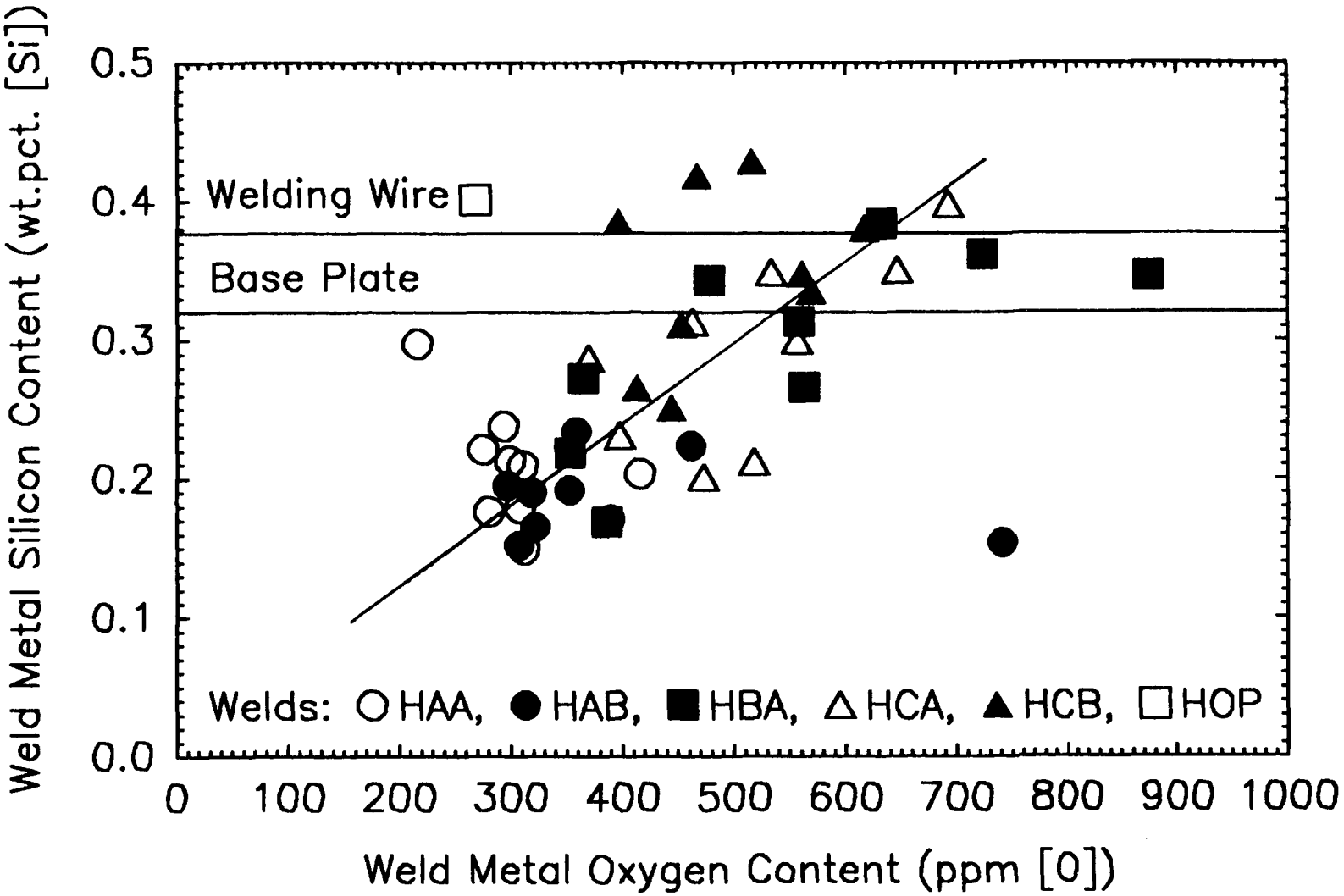

Figure 14. Weld metal silicon content plotted as a function of weld metal oxygen content.

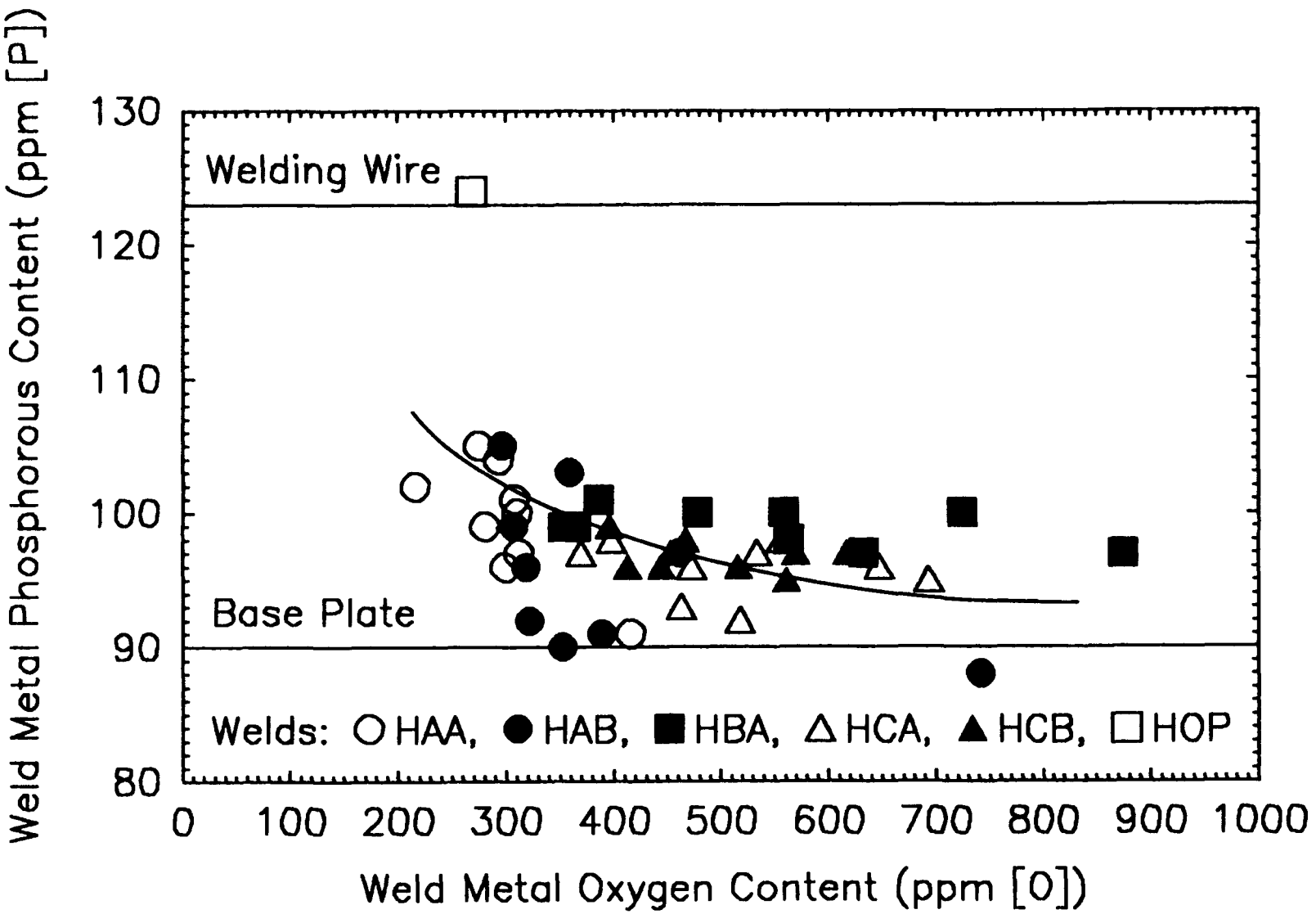

Figure 15. Weld metal phosphorus content plotted as a function of weld metal oxygen content.

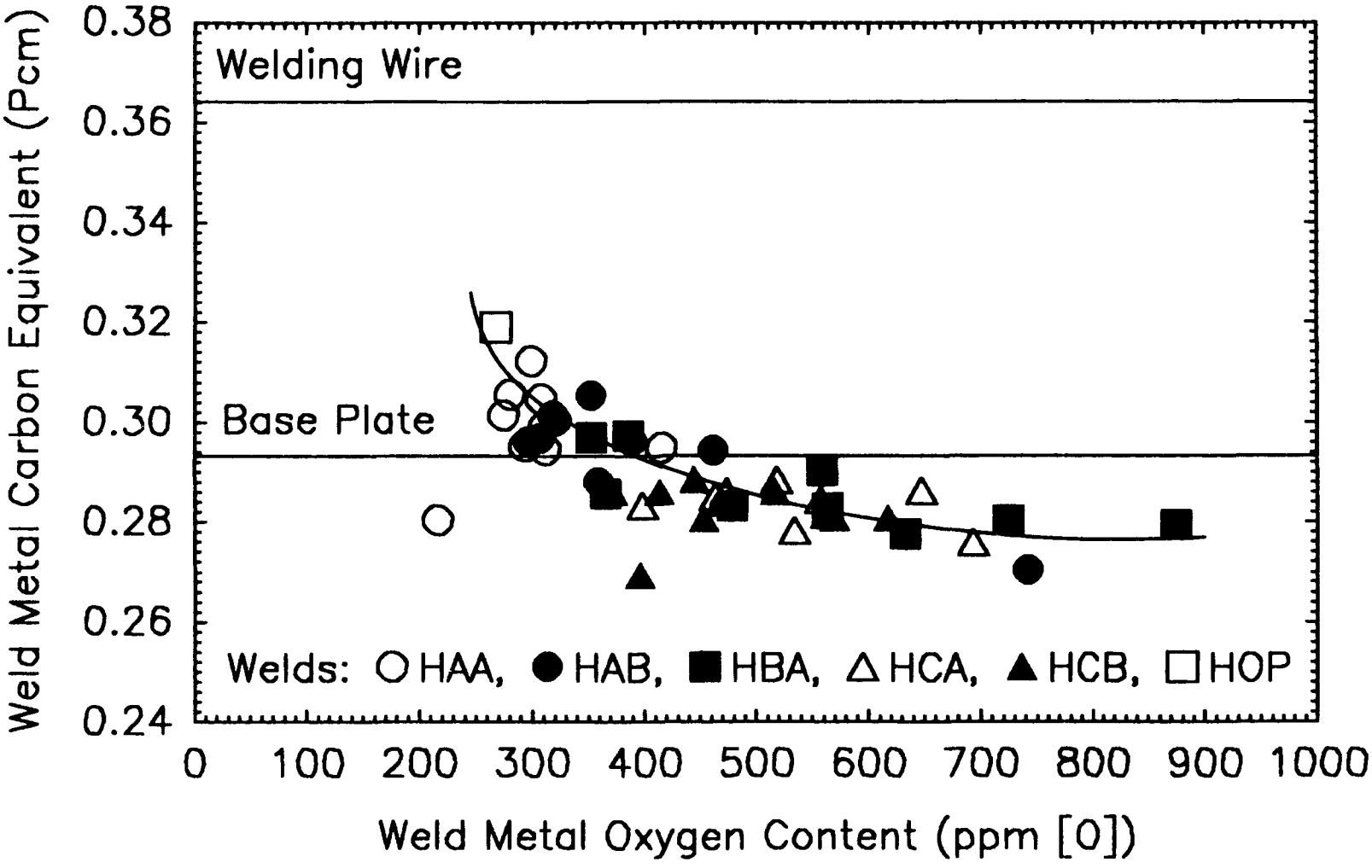

Figure 16. Weld metal P_{cm} plotted as a function of weld metal oxygen content.

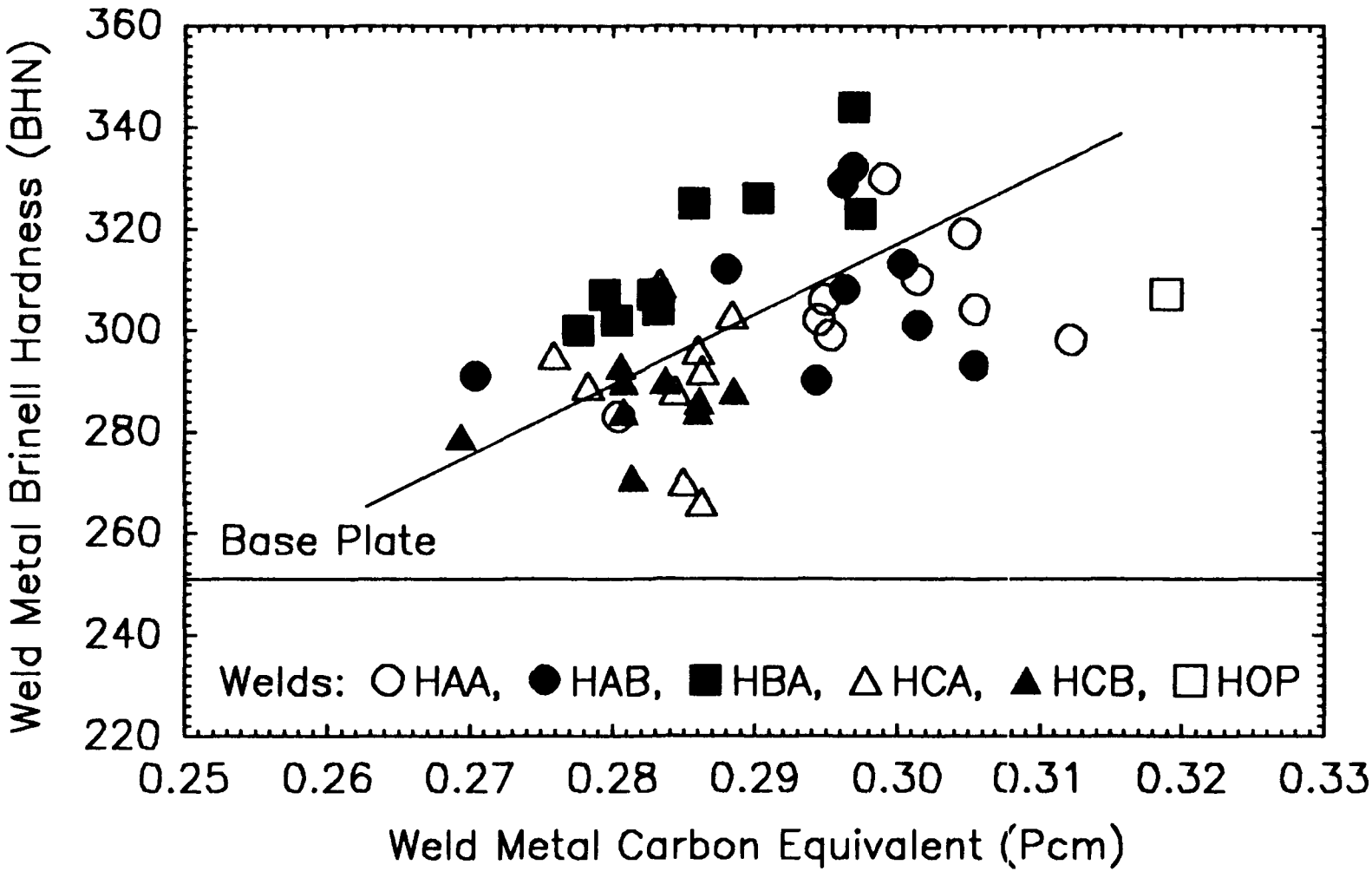

Figure 17. Weld metal Brinell hardness plotted as a function of weld metal P_{cm}.

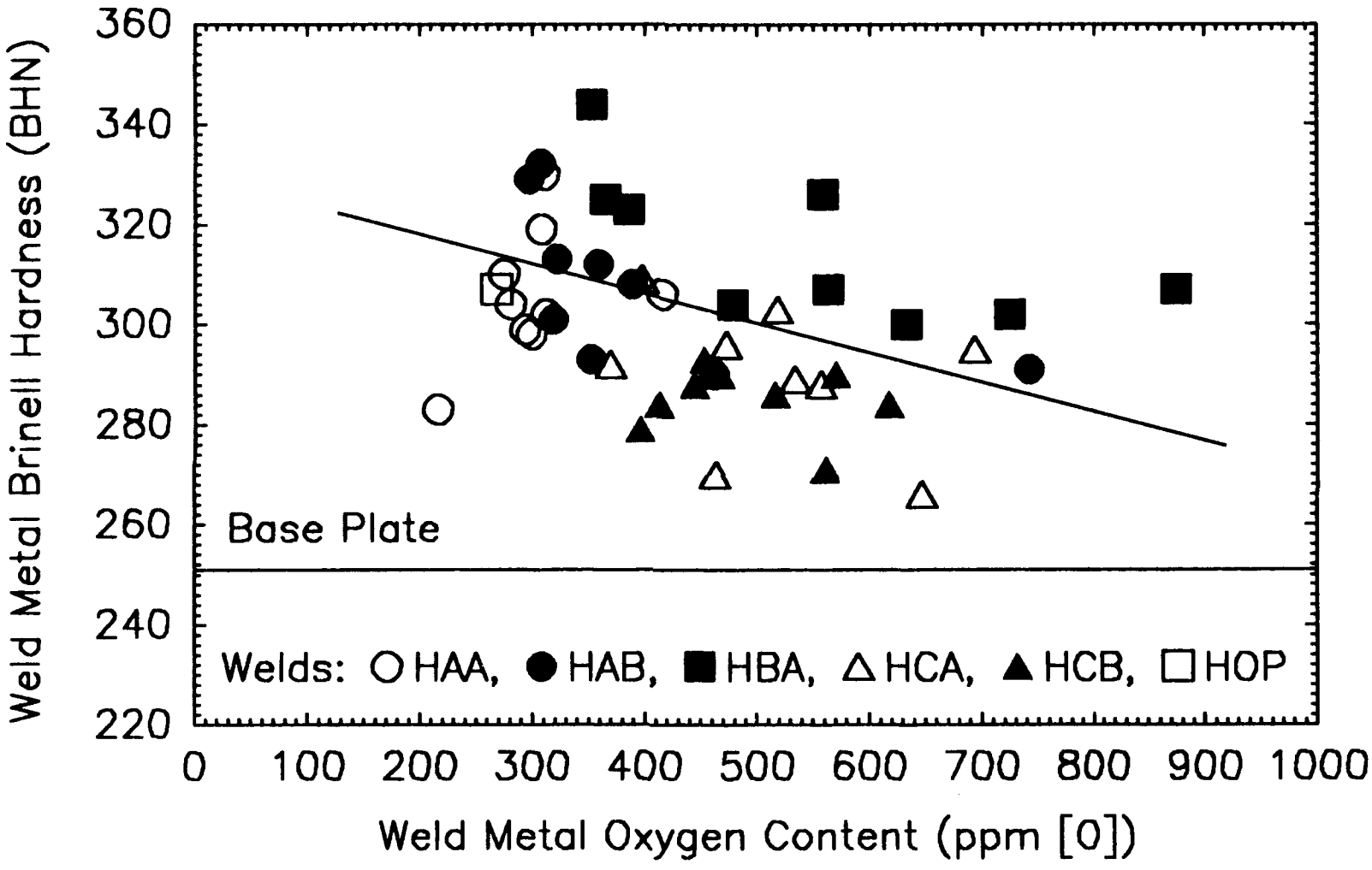

Figure 18. Weld metal Brinell hardness plotted as a function of weld metal oxygen content.

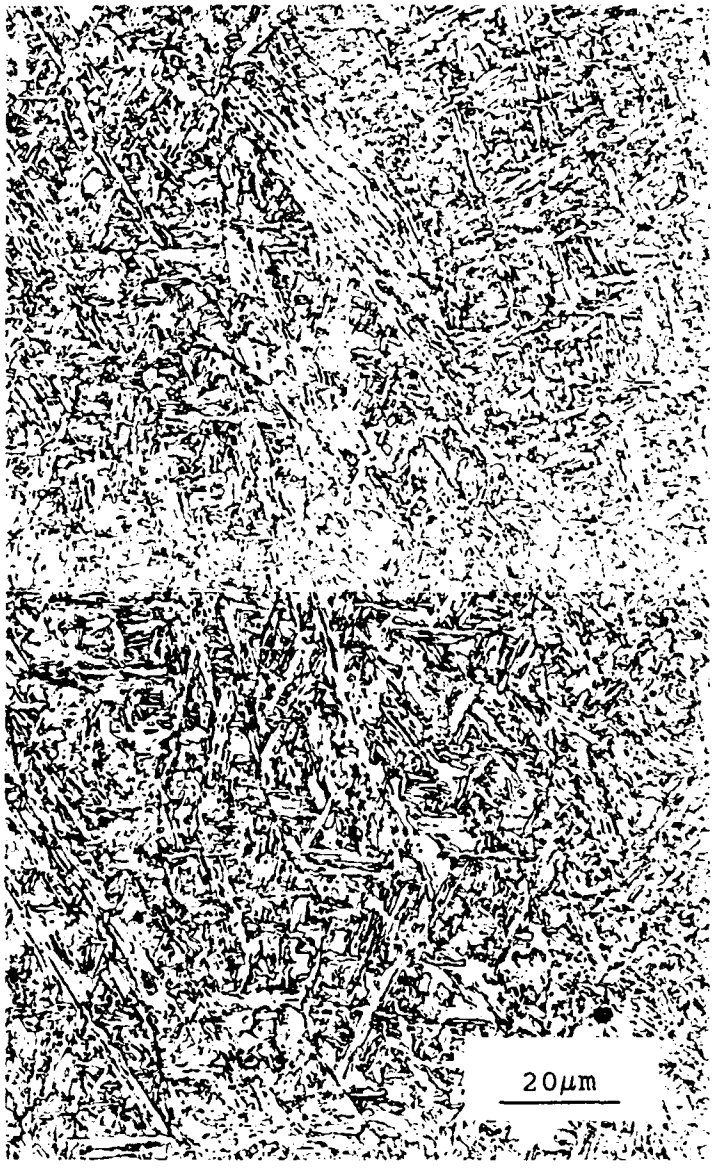

Figure 19. Light micrograph of weld HAA3.

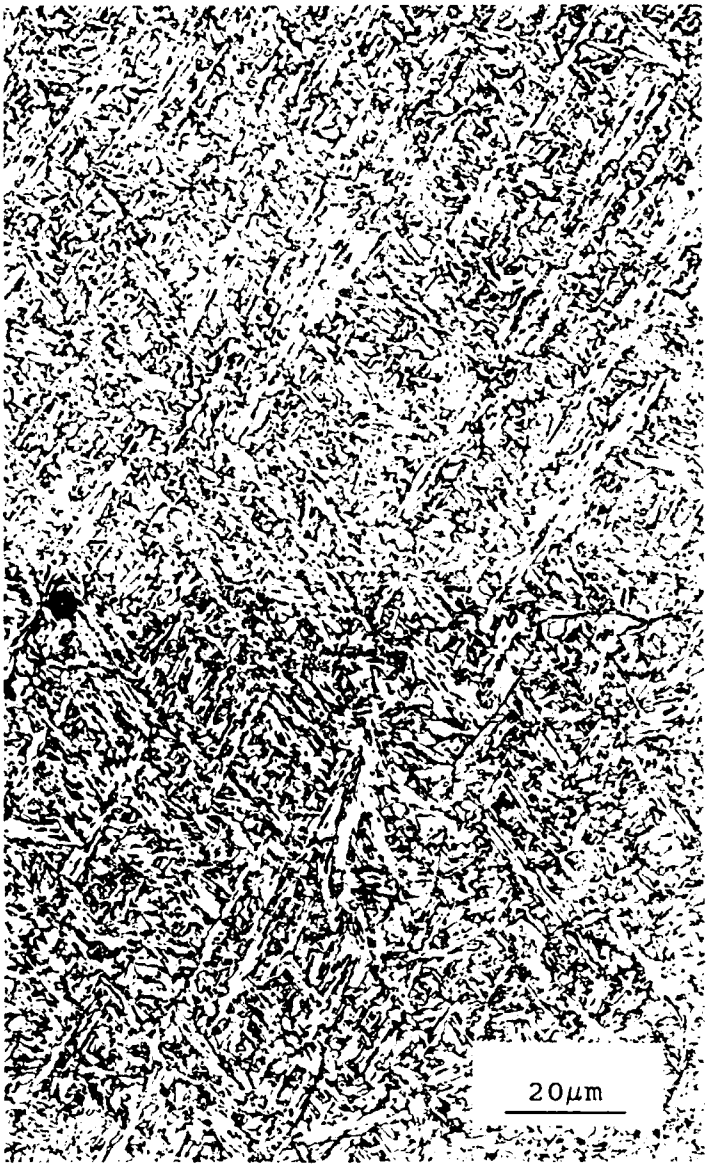

Figure 20. Light micrograph of weld HAA7.

Figure 21. Light micrograph of weld HAB3.

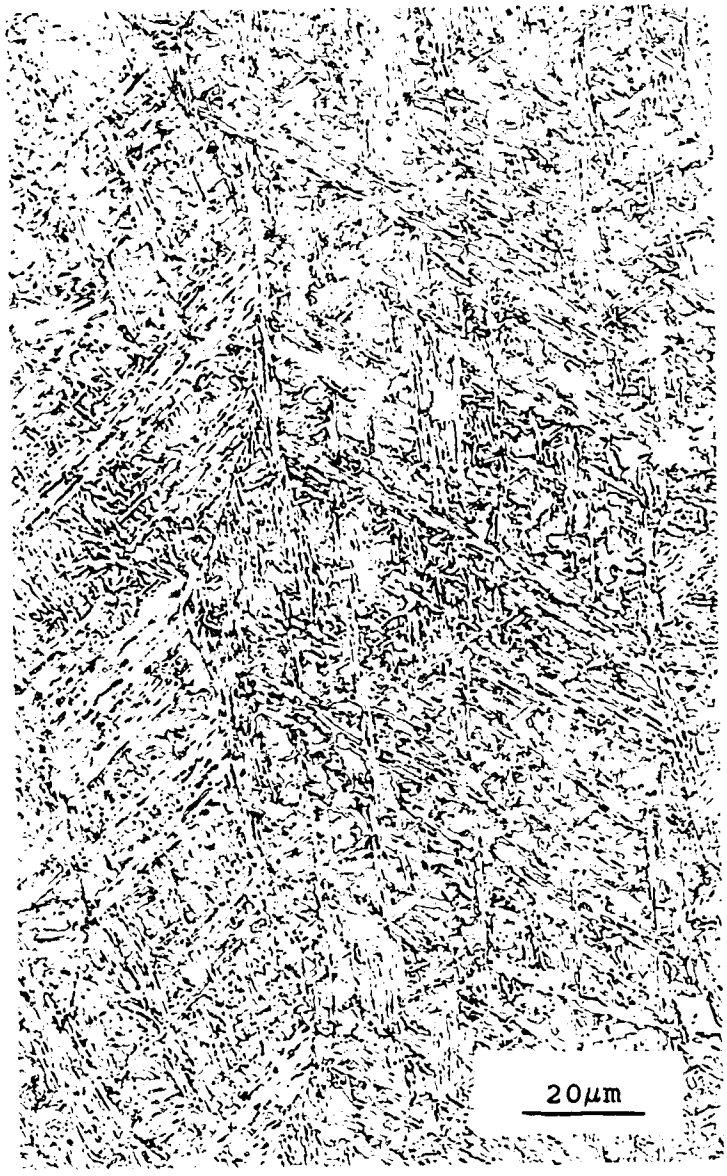

Figure 22. Light micrograph of weld HAB7.

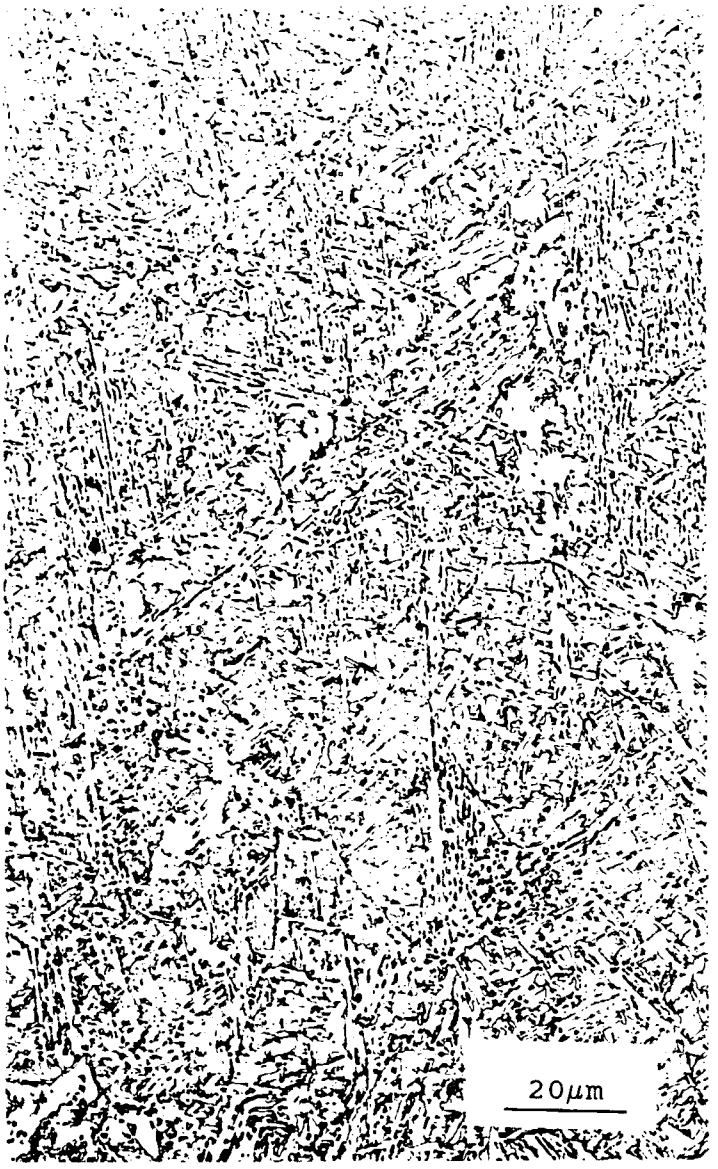

Figure 23. Light micrograph of weld HCA2.

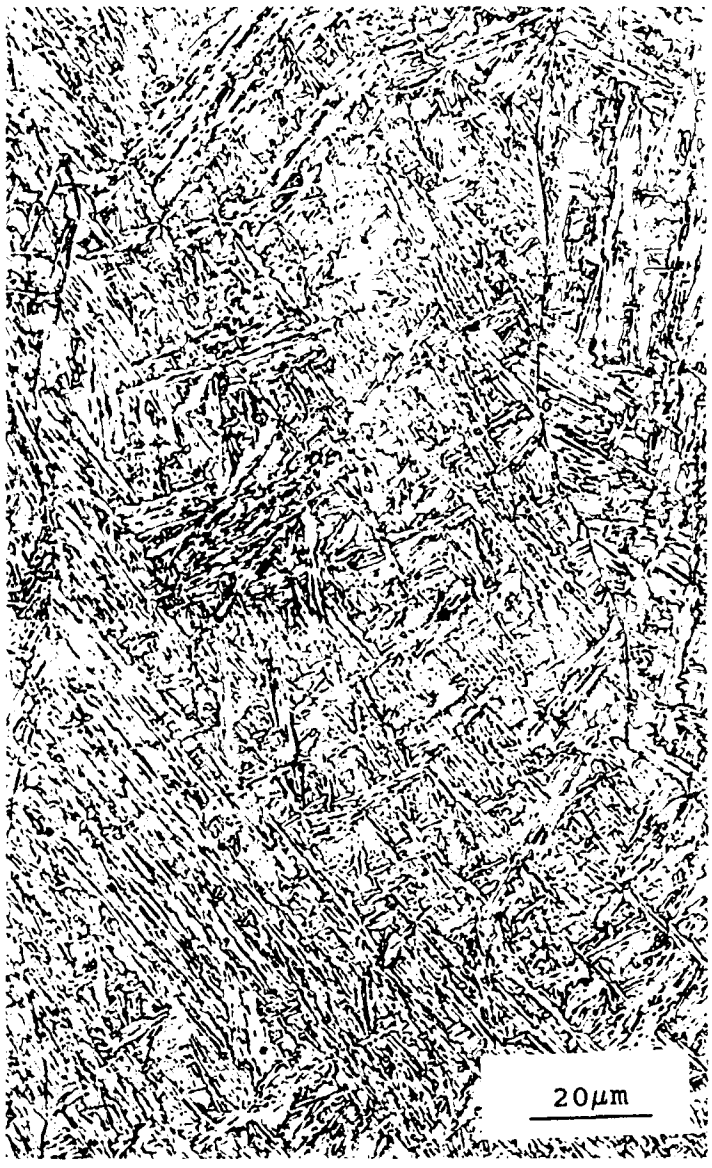

Figure 24. Light micrograph of weld HCA7.

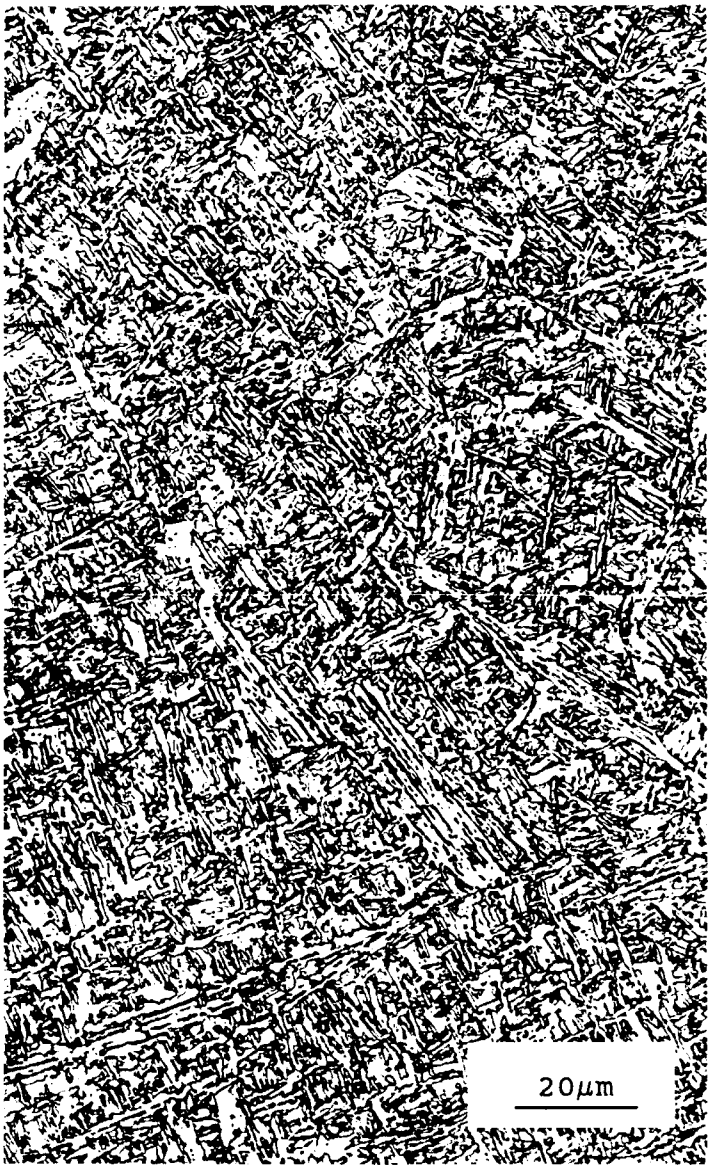

Figure 25. Light micrograph of weld HCB2.

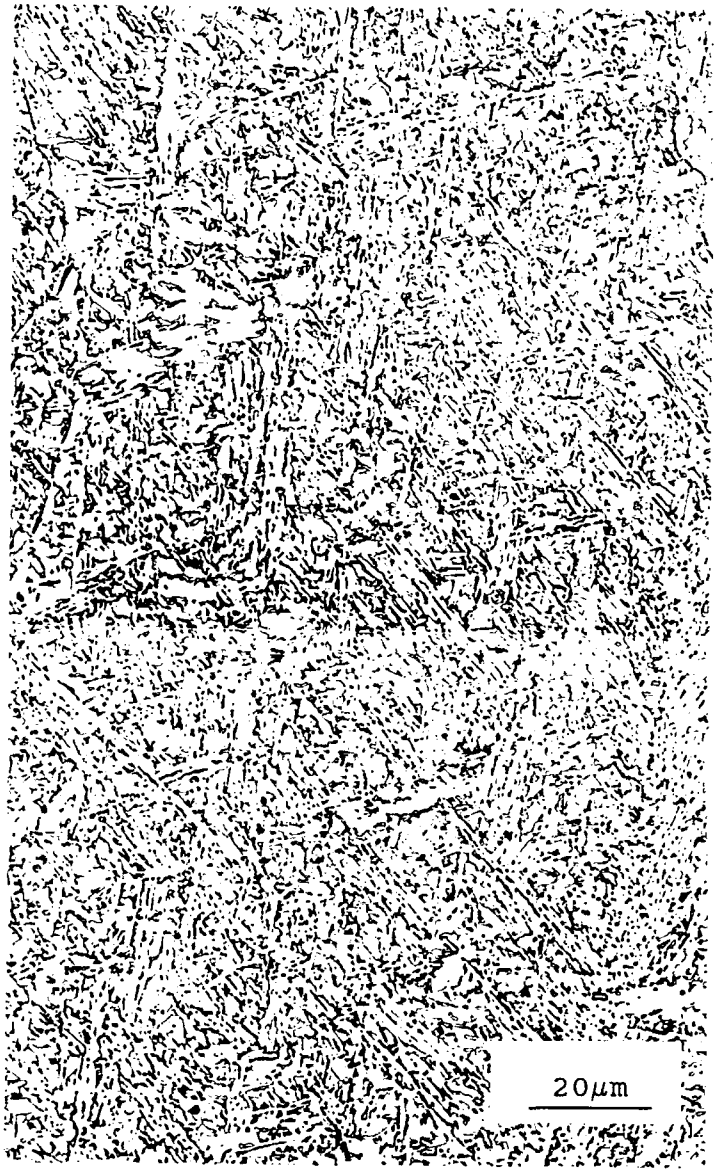

Figure 26. Light micrograph of weld HCB7.

Figure 27. Light micrograph of HSLA-100 steel showing the martensitic-bainitic microstructure.

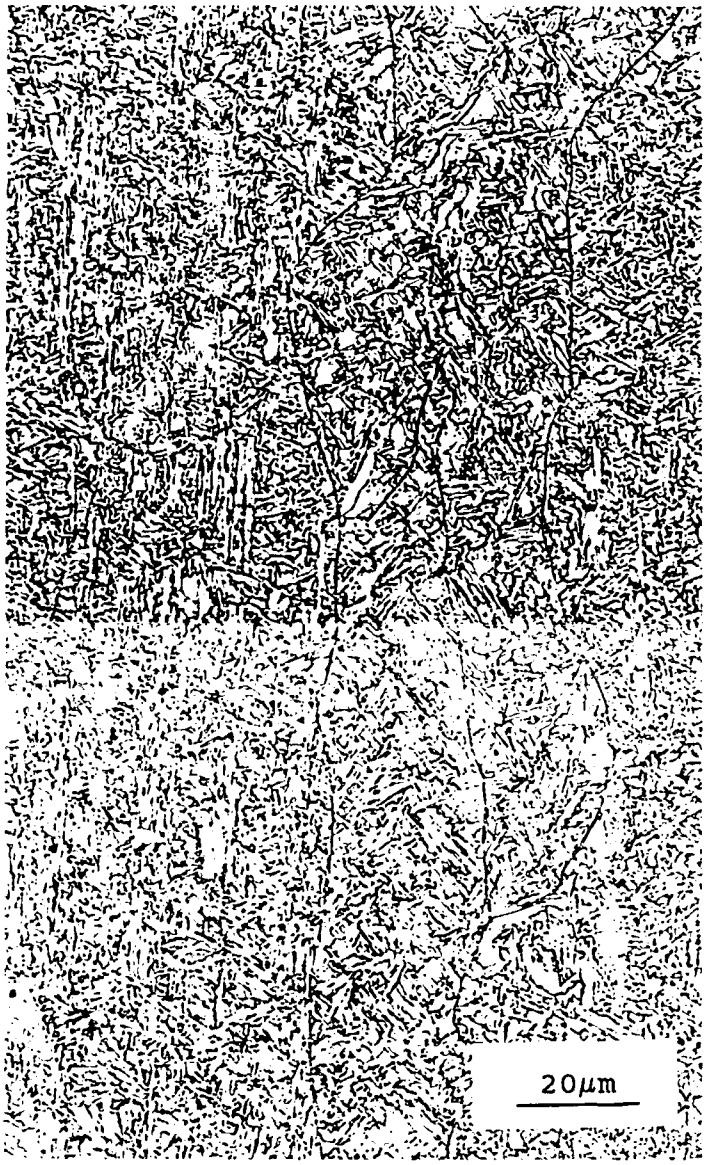

Figure 28. Light micrograph of weld HOP made using the Oerlikon OP121TT welding flux.

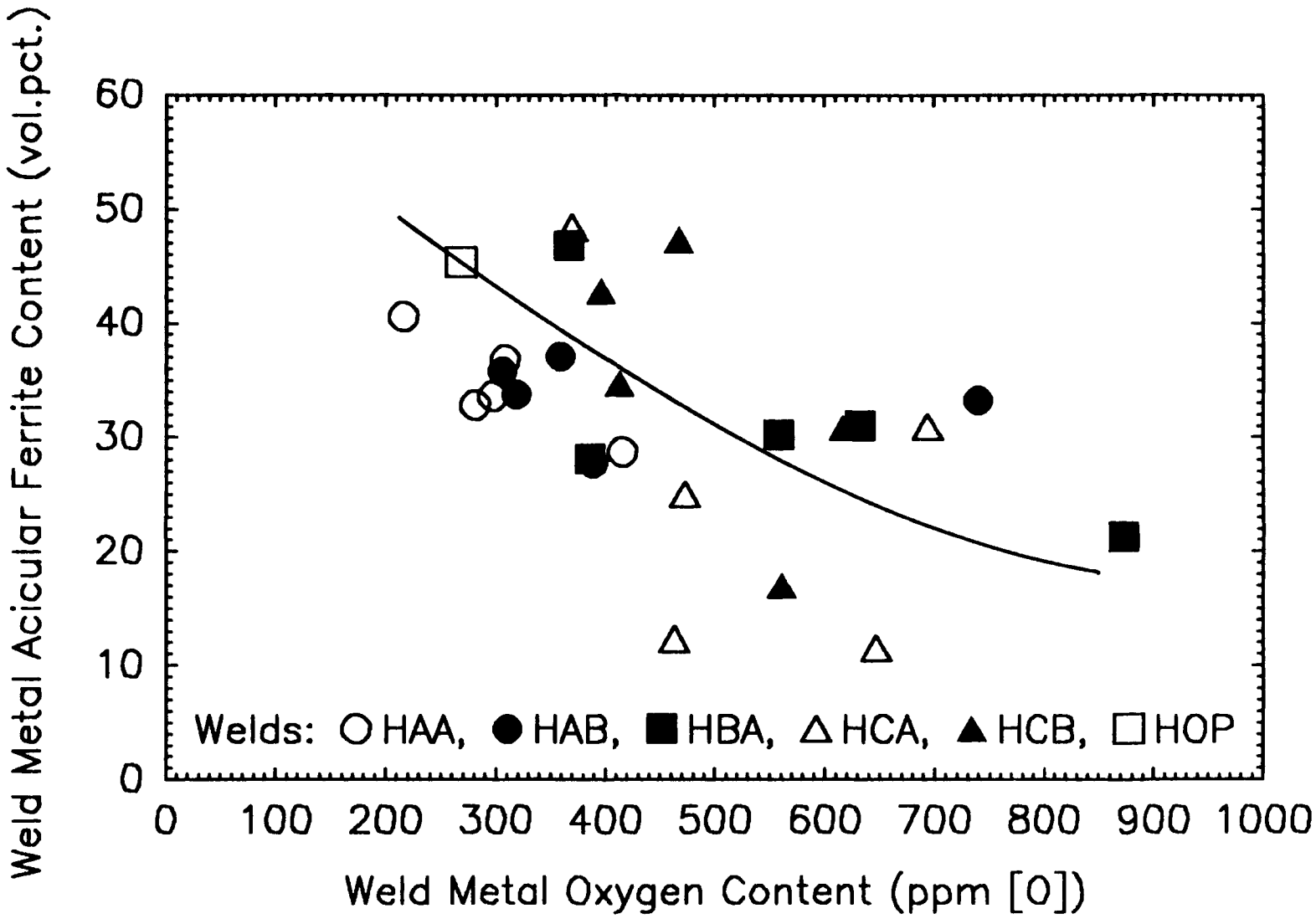

Figure 29. Volume fraction of acicular ferrite in HSLA-100 steel weld metal plotted as a function of weld metal oxygen content.

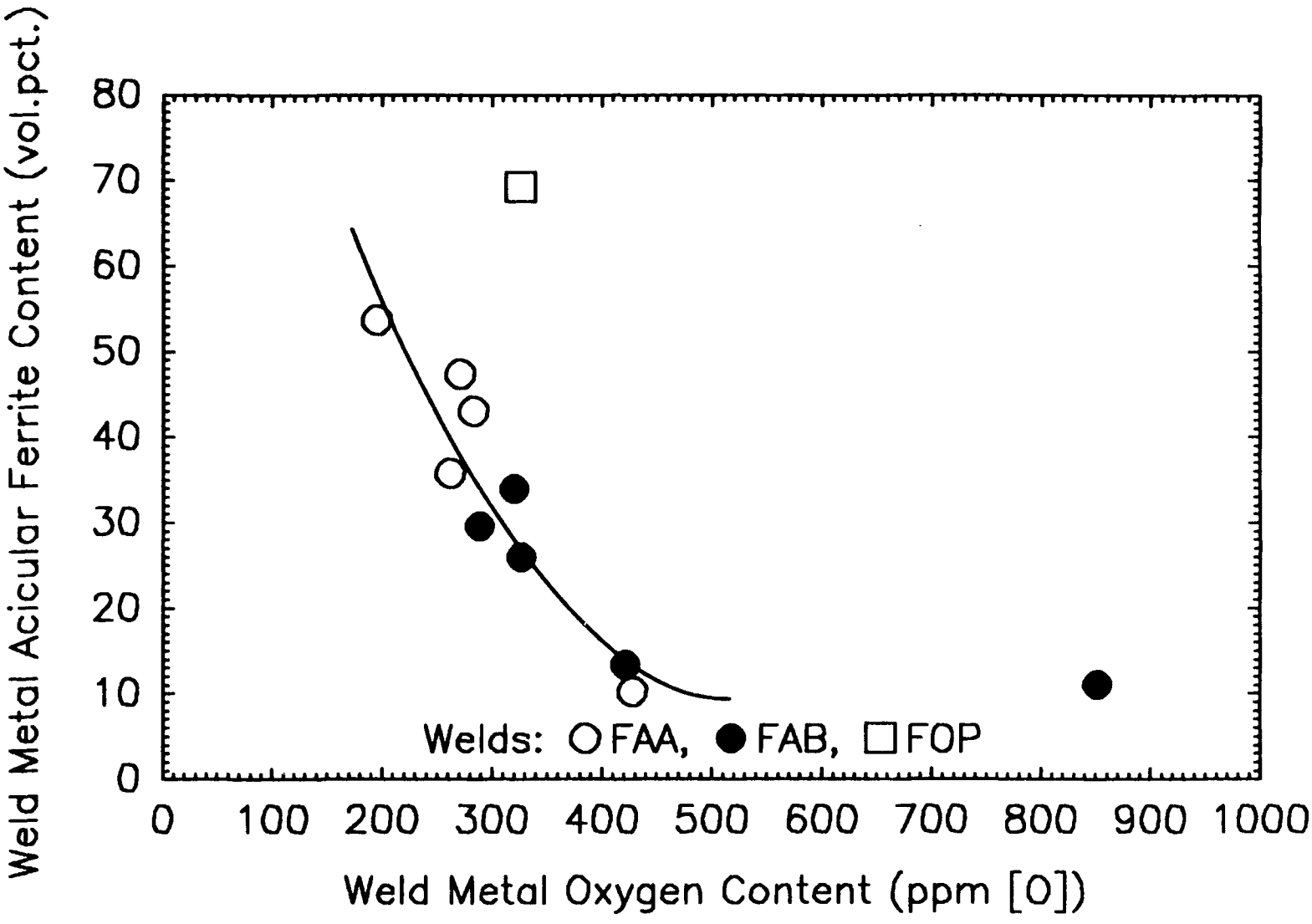

Figure 30. Volume fraction of acicular ferrite in AISI 1018 steel weld metal plotted as a function of weld metal oxygen content.

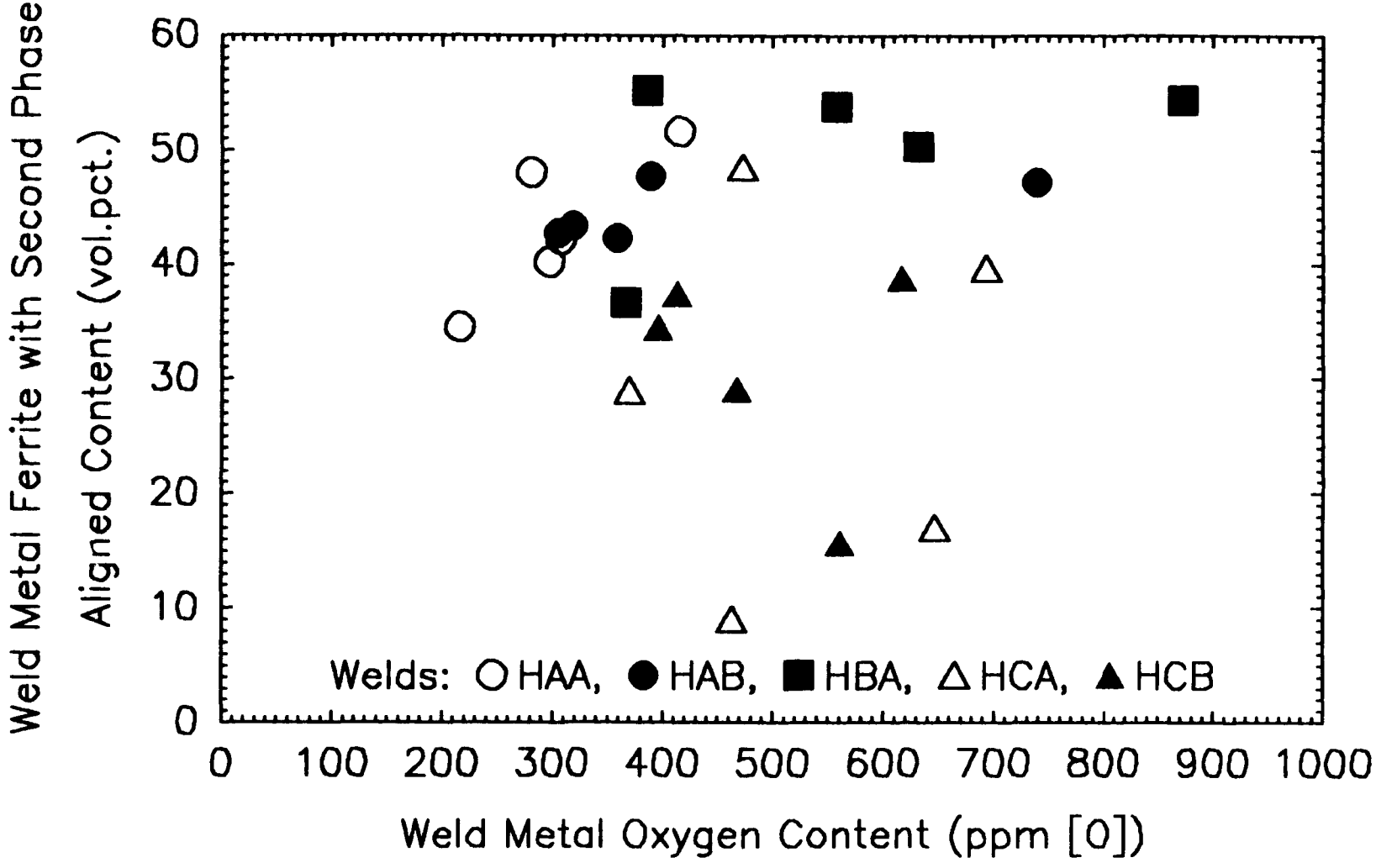

Figure 31. Volume fraction of ferrite with second phase aligned plotted as a function of weld metal oxygen content in the HSLA-100 steel welds.

dicates that the amount of ferrite with second phase aligned increased with weld metal oxygen content. However, the scatter in the experimental data was again considerable. The results from the low carbon steel welds showed a significantly better correlation that the volume fraction of ferrite with second phase aligned increased with weld metal oxygen content, Figure 32. When the volume fraction of ferrite with second phase aligned was plotted versus the amount of acicular ferrite, a clear trend was observed, Figure 33. As weld metal oxygen increased, ferrite with aligned second phase increased at the cost of acicular ferrite. This was again confirmed by the low carbon steel welding experiments, Figure 34. Excellent correlation between acicular ferrite and ferrite with aligned second phase was observed.

The discussion above shows that the quasi-ternary experimental fluxes were capable of modifying the microstructure of the HSLA-100 steel welds and that the flux oxygen potential determines the relative amounts of acicular ferrite and ferrite with second phase aligned.

II.1.2.5. Weld Metal Mechanical Properties

Some selected Charpy-V-notch testing results are reported in Table IV. Figures 35 to 39 illustrate further the influence of the experimental fluxes on weld metal toughness. As weld metal oxygen increased, result of the higher flux oxygen potential, the energy absorbed during Charpy-V-notch testing was observed to decrease, Figure 35. Increasing volume fraction of acicular ferrite, decreasing oxygen in the weld metal, improved the toughness, Figure 36. The non-parallel nature of the acicular ferrite laths usually exhibit high resistance to crack propagation and increase weld metal toughness.

P_{cm} also seems to play an important role in the determination of weld metal toughness. There appears to be a threshold value of P_{cm}, approximately 0.29 wt.pct, beyond which a minimum Charpy-V-notch energy of 20 ft-lb is observed, Figure 37. This threshold point also corresponds to a weld metal oxygen content of 300 ppm, Figure 16. Careful examination of Figure 35, however, seems to indicate that if the weld metal oxygen exceeds 400 ppm, the energy absorbed during Charpy-V-notch testing also approaches a minimum. As such, the flux that will provide optimal performance in terms of microstructure and toughness is expected to result in a weld metal oxygen content between 300 to 400 ppm. Several fluxes from the systems AB, BA, CA, and CB will meet the conditions above and will be tested further in shielded metal arc welding.

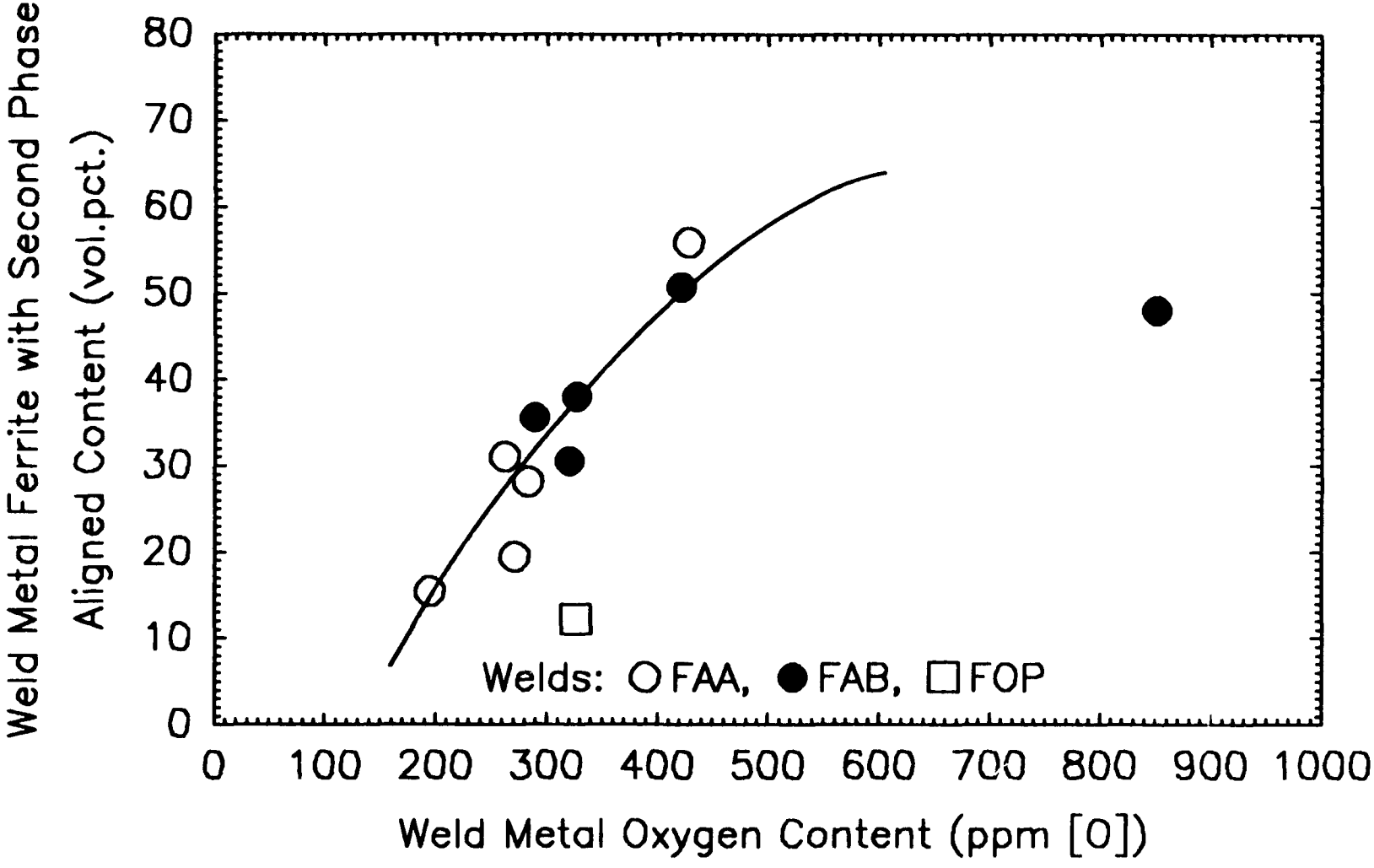

Figure 32. Volume fraction of ferrite with second phase aligned plotted as a function of weld metal oxygen content in the AISI 1018 steel welds.

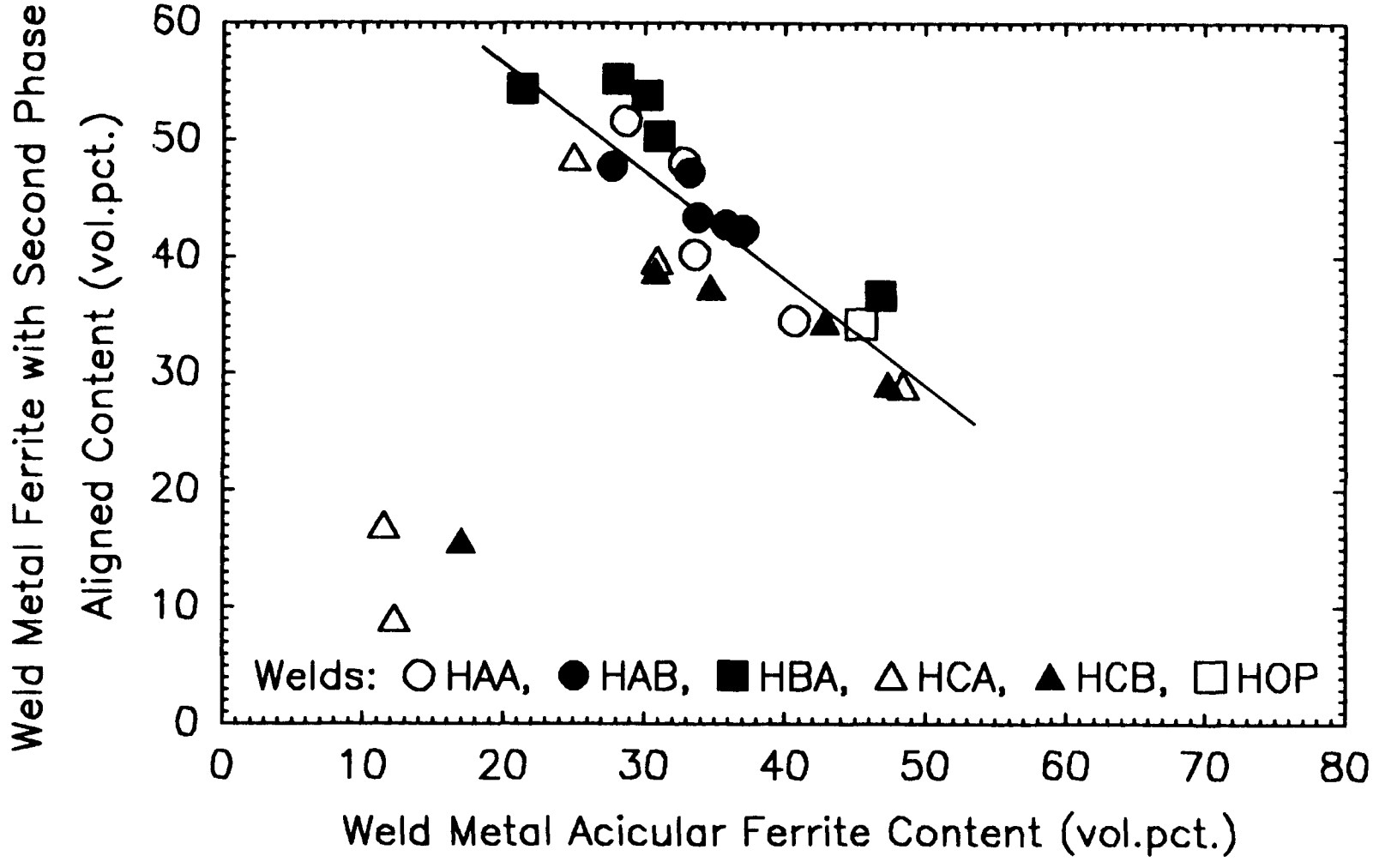

Figure 33. Volume fraction of ferrite with second phase aligned plotted as a function of the amount of acicular ferrite in the HSLA-100 steel weld metals.

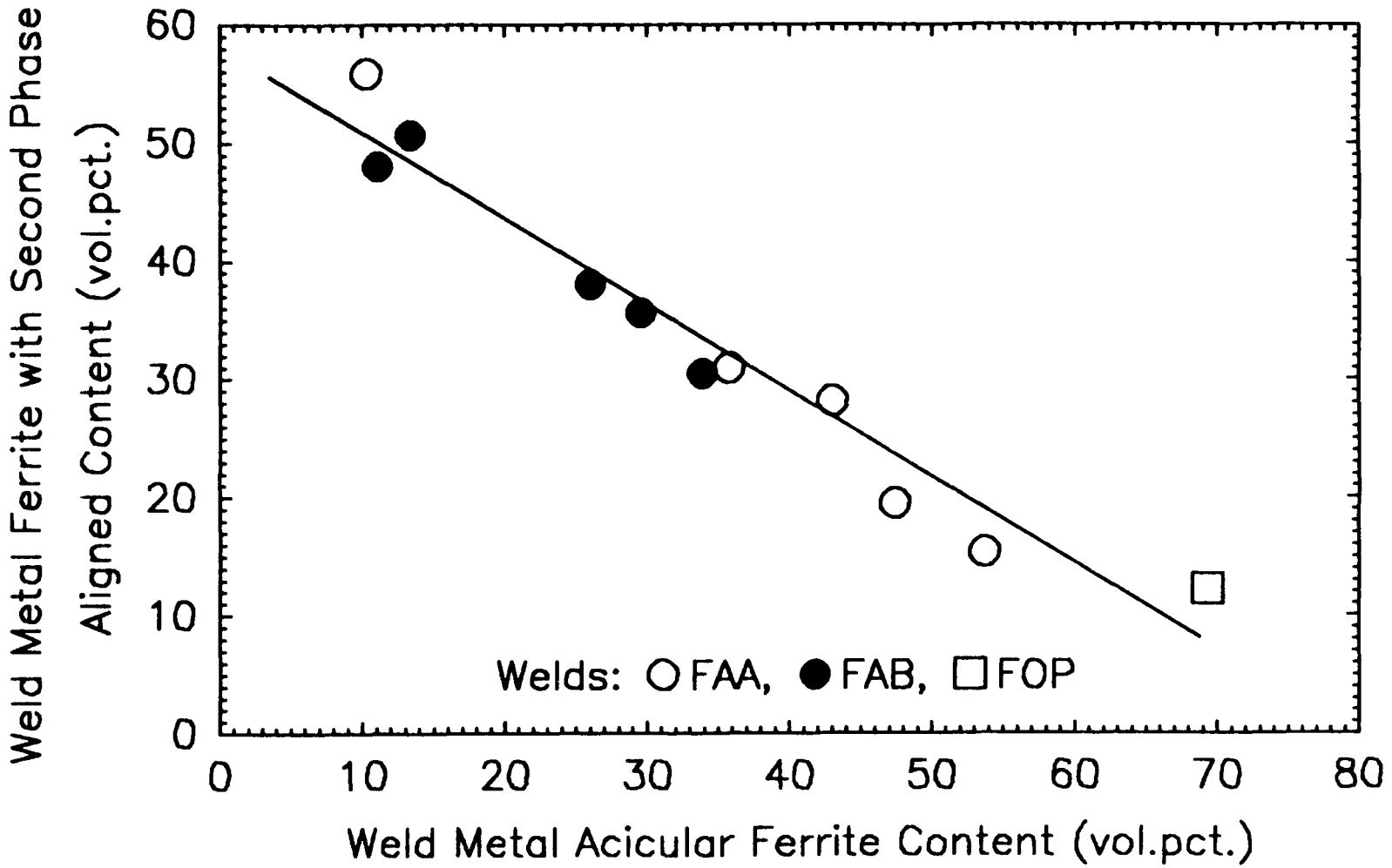

Figure 34. Volume fraction of ferrite with second phase aligned plotted as a function of the amount of acicular ferrite in the AISI 1018 steel weld metals.

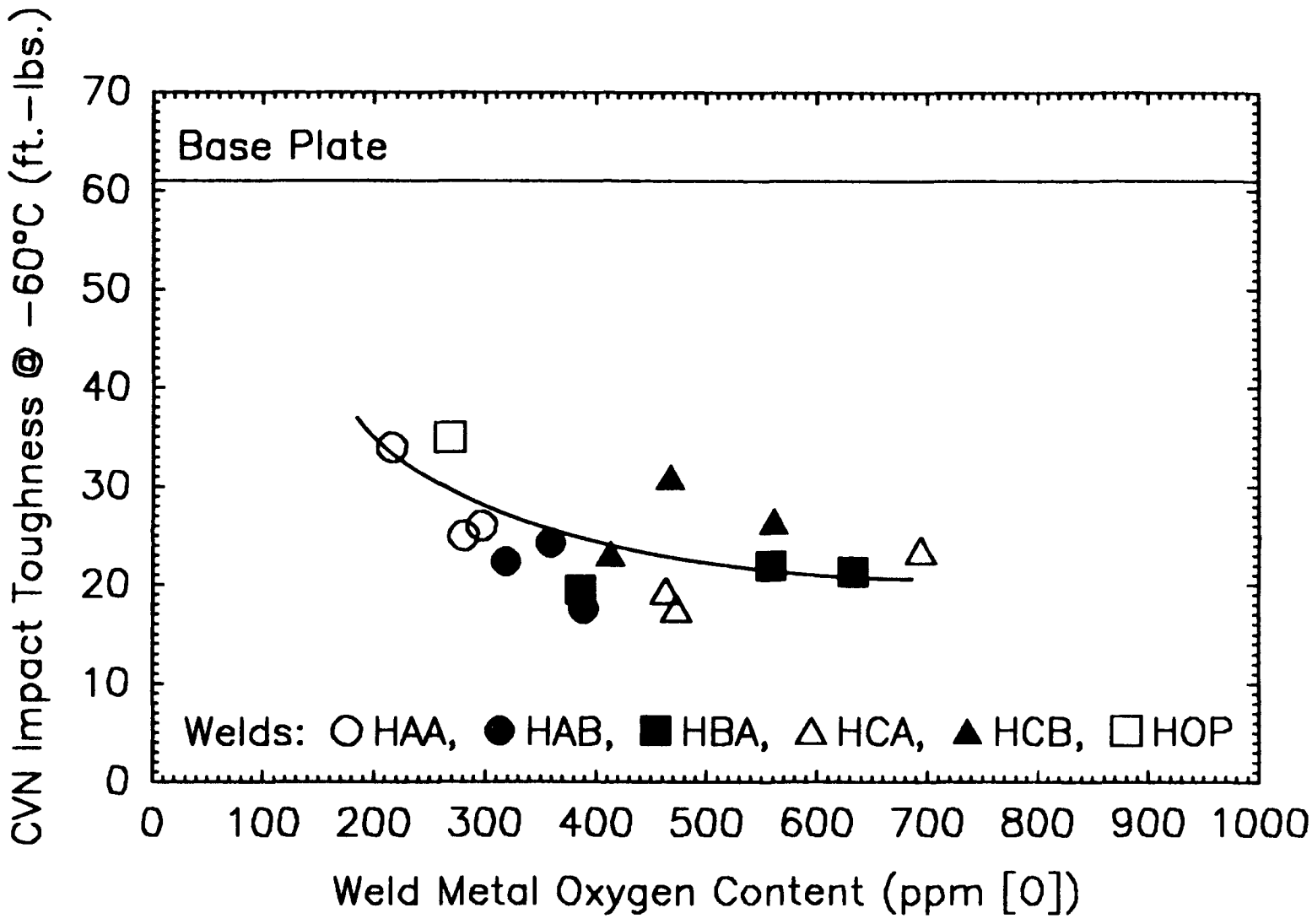

Figure 35. Charpy-V-notch impact toughness plotted as a function of the weld metal oxygen content.

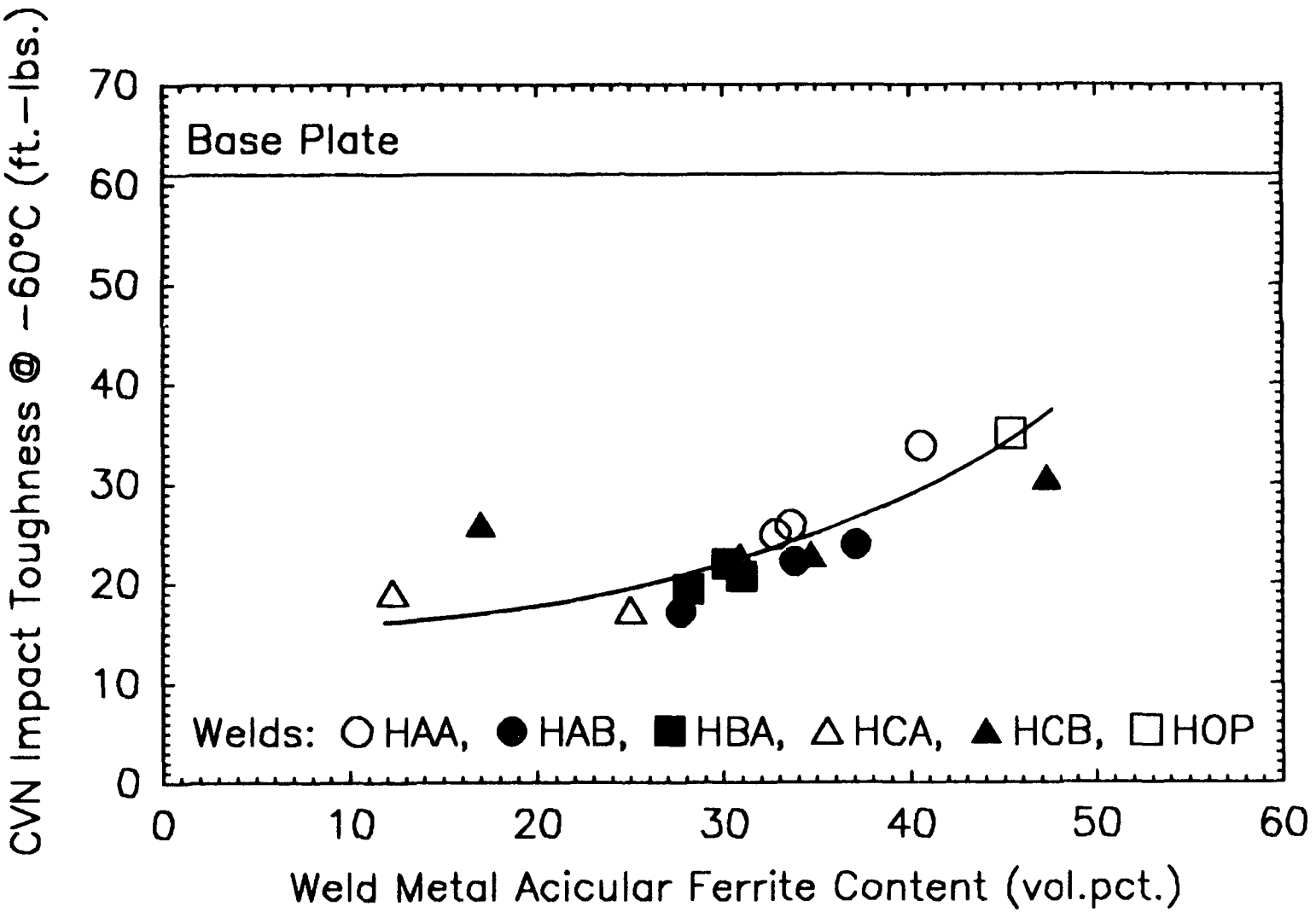

Figure 36. Charpy-V-notch impact toughness plotted as a function of the weld metal acicular ferrite content.

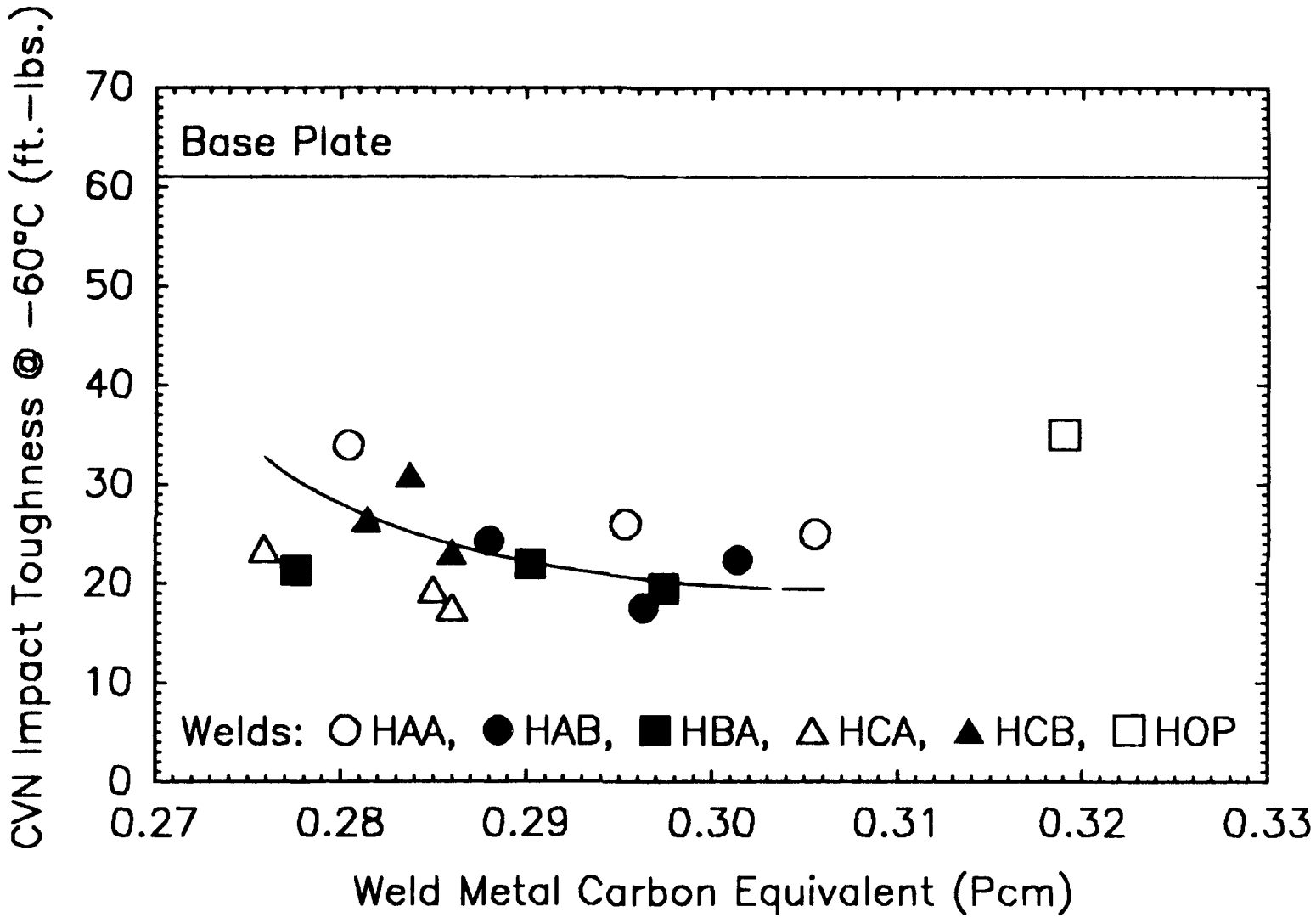

Figure 37. Charpy-V-notch impact toughness plotted as a function of the weld metal P_{cm} value.

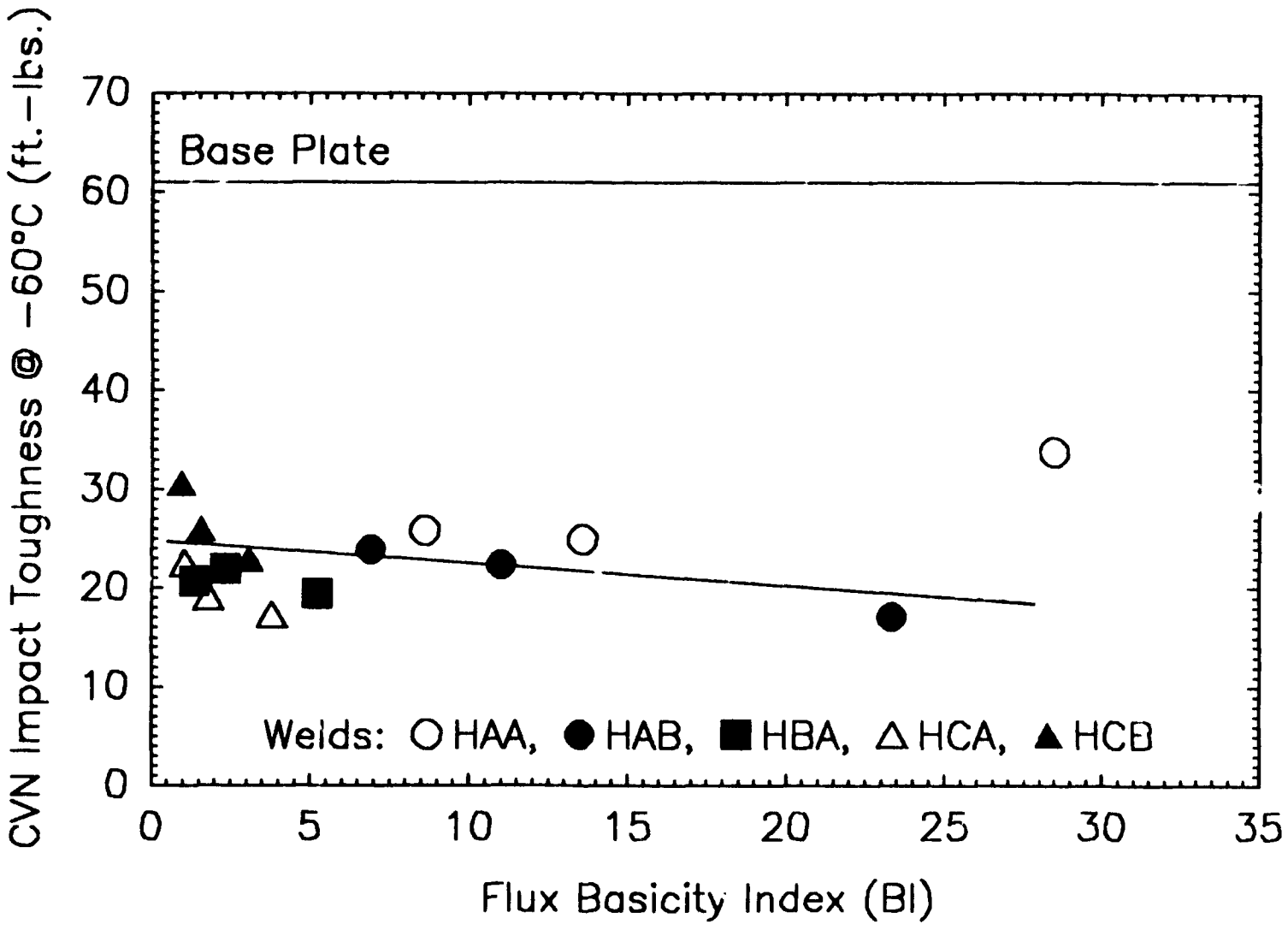

Figure 38. Charpy-V-notch impact toughness plotted as a function of the flux basicity index, B_I.

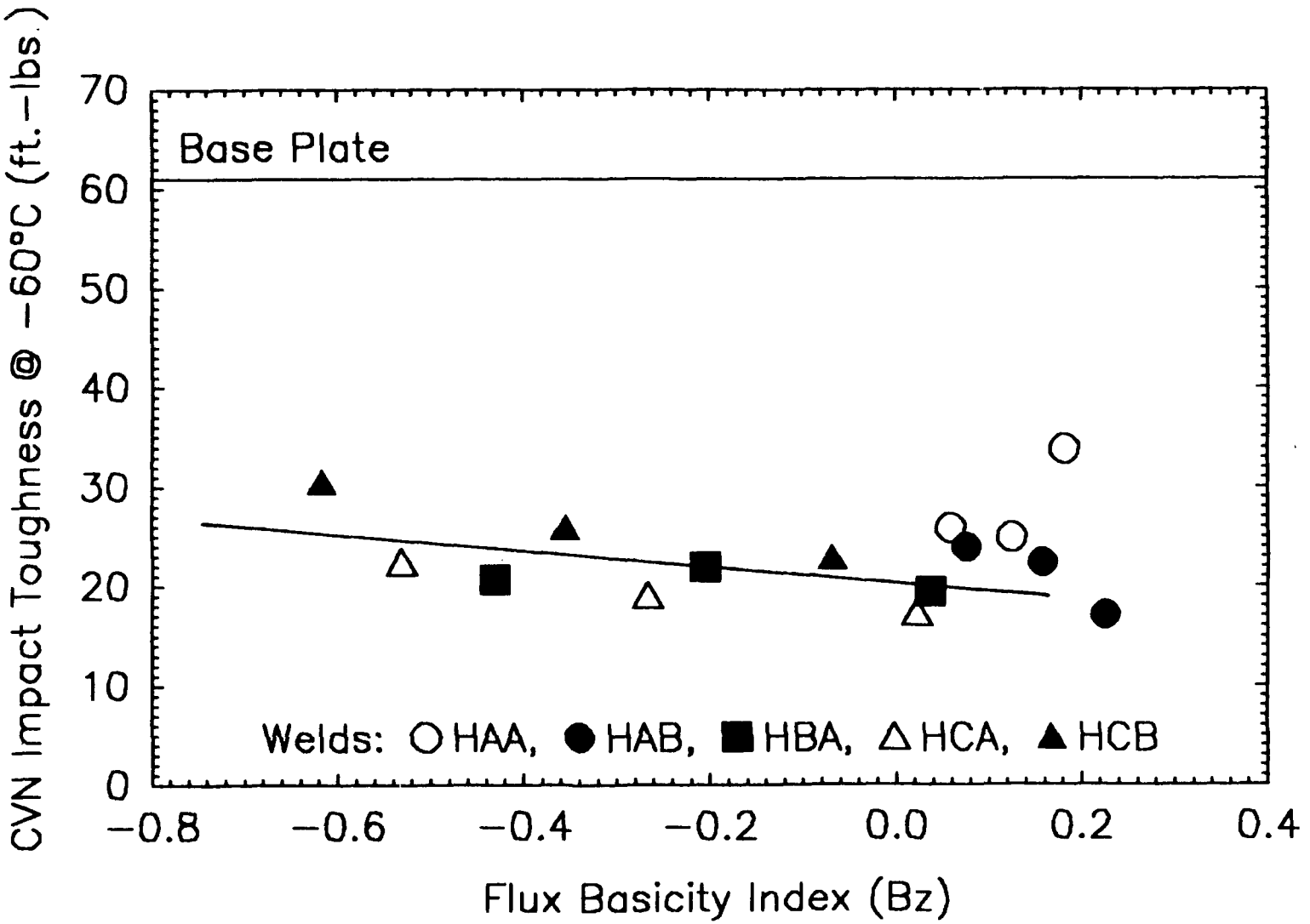

Figure 39. Charpy-V-notch impact toughness plotted as a function of the Zeke basicity index, B_z.

Again, basicity index should not be used to correlate microstructure nor mechanical properties. Figures 38 and 39 conclude similar observations.

II.2. Shielded Metal Arc Welding

II.2.1. Experimental Procedure

Based on the results obtained in the submerged arc welding matrix reported in the previous section, four candidate shielded metal arc electrode coating compositions were selected. Fluxes AA7 and CB2 produced welds that exhibited the highest toughness using sub-sized Charpy impact specimens. A larger relative volume fraction ratio of acicular ferrite to undesirable constituents such as ferrite with aligned second phase and primary ferrite was observed in welds prepared with fluxes AA7 and CB2. Fluxes CA9 and CB9 were also selected based on correlations determined by Charpy-V-notch testing and microstructural analysis. The compositions of the chosen fluxes are shown in Table I.

The high purity grade chemicals used during the submerged arc welding flux investigation were very fine (-325 Tyler mesh) and did not produce an acceptable electrode coating during extrusion. Good extrudability was achieved only when a large amount of binder was used. The use of fine powders also resulted in a rough surface finish and cracking of coatings after drying. Even though fine particles provided good plasticity during extrusion, drying was not uniform; cracked coatings consequently resulted. Coarse particles, while not as extrudable, allowed for fast and uniform drying of the coating. A combination of coarser flux ingredients (-40 to +200 # Tyler mesh) required less binder and yielded electrodes with a crack-free surface, visually comparable to many commercial electrodes. Coatings must have a proper balance of particle sizes to ensure the following: ease of extrusion, adequate strength to withstand handling, and morphology which permits immediate and continuous drying. A 50/50 wt. pct. mixture of potassium silicate and sodium silicate binders was used to increase the coating resistance to moisture pickup after baking, and to stabilize the arc during welding.

Initially, the dry flux components were weighed and mixed in a dry mixing blender. The binder was then weighed and incrementally added into the dry mix and blended by hand until an extrudable flux was obtained. Mixing by hand allowed for the determination of the appropriate amount of binder required for extrusion, through the "feel" of the consistency of the mix. When the right amount of binder has been added, the wet mix exhibited a uniform plasticity, indicating

the right consistency for extrusion. At this time, the amount of binder added to the formulation was recorded. No known testing method can reproduce the tactile sensing of the flux by hand. A drop wedge test, similar to that used in foundry sand testing, is being developed in this study and may eventually replace the empirical approach of determining the optimal plasticity point by tactile sensing. After an extrudable mixture was obtained, the wet flux was compacted into a cylindrical slug and placed into the extruding press. Extrusion pressure (ram speed) was adjusted until a smooth and uniform coating was produced. The coating eccentricity was measured and the centering of the electrode relative to the coating adjusted. After extrusion, the electrodes were allowed to air dry before baking at 450°C for one hour in an argon atmosphere. A baking schedule of 450°C for one hour is reported to yield weld metal diffusible hydrogen levels of less than 5 ml H_2 per 100 g weld metal at standard temperature and pressure (STP) (Ref. 4). The argon atmosphere was selected because evidence of oxidation of the core electrode and iron powder in the flux coating was observed when the electrodes were baked in air. After baking, the electrodes were stored in a holding oven at 180°C.

It was the intent of this study to use the Airco AX-140 welding wire as core electrode for the extrusion of shielded metal arc electrodes, so that results of the SMA welding results could be compared directly with those obtained in SA welding. Unfortunately, the Airco AX-140 wire used in the submerged arc welding research was unavailable in 1/8" (3.2 mm) diameter because commercial production was discontinued. An alternate alloyed steel core electrode (ER100S-1) was used. The composition of this electrode is shown in Table V. Notice that the composition of ER100-S1 core rod is slightly different from that of the Airco AX-140 electrode used in the submerged arc welding experiments.

Coating moisture tests were conducted according to AWS A5.1-81 Section 13.12 (Specifications for covered carbon steel arc welding electrodes) (Ref. 5), utilizing the experimental apparatus is shown in Figure 40. The coating was combusted in

Table V. Chemical composition (in wt. pct.) of the ER100S-1 core electrode used in the shielded metal arc welding experiments.

Core electrode ID	C	Mn	Si	P	S	Ni	Mo	Cr	Cu	V	Ti
ER100-S1	0.061	1.35	0.51	0.006	0.006	1.95	0.46	0.078	0.11	0.045	0.020

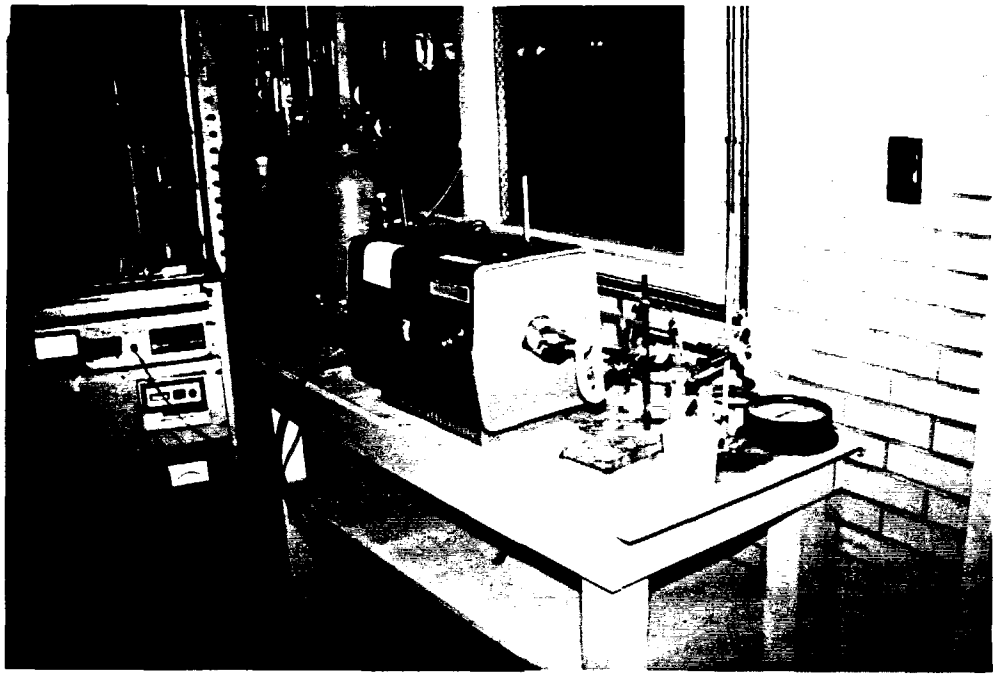

Figure 40. Experimental apparatus for the determination of electrode coating moisture content.

a stream of pure dry oxygen between 900 to 1000°C, and the moisture evolved from the coating was absorbed in a glass tube that contained anhydrous magnesium perchlorate, $Mg(ClO_4)_2$. The amount of moisture absorbed by the anhydrous magnesium perchlorate was determined by the weight change of the contents of the glass tube. A coating moisture level of less than 0.2% was observed when the baking schedule described earlier was followed. Data reported in the literature (Ref. 4) states that a coating moisture level of 0.2% is necessary to achieve very low hydrogen levels in the weld metal.

Prior to welding, the test plates were prepared following the same procedure described in the submerged arc welding section. Bead-on-plate welds were made using the automatic shielded metal arc welding system developed. The use of this system, shown in Figures 41a and 41b, produced high quality welds and eliminated the many inconsistencies introduced during manual welding. Current and voltages were chosen to provide optimal slag coverage and appropriate bead morphology. A minimum voltage of 30 volts was established for the CB2 electrode. Currents higher than 120 amps caused the slag to burn off, thereby exposing the hot weld bead to the atmosphere. The heat input of these welds varied between 1.1 to 1.4 kJ/mm (27.9 to 35.6 kJ/in.).

A Leco image analyzer was used to determine the dilution and bead morphology of the six SMA welds produced. The image analyzer provided more accurate measurements of the relative areas used to calculate dilution.

Diffusible hydrogen was measured according to AWS A4.3-86 (Standard Methods for Determination of the Diffusible Hydrogen Content of Martensitic, Bainitic, and Ferritic Weld Metal produced by Arc Welding) (Ref. 4) using the diffusible hydrogen collection equipment shown in Figure 42. The welds were produced on A36 steel test coupons. Immediately after the arc was extinguished the weld was quenched in ice water and transferred to liquid nitrogen for further processing and storage. Diffusible hydrogen was collected in mercury-filled glass eudiometer tubes maintained at 45°C for 72 hours. Prior to insertion into the eudiometer tubes, the test coupons were warmed to 0°C, rinsed in acetone, and blown dry.

II.2.2. Results and Discussion

II.2.2.1. Electrode Weldability

When basic electrodes are used, a cup (arc barrel) is formed at the tip of the electrode which protects the arc column from the atmosphere during welding. The

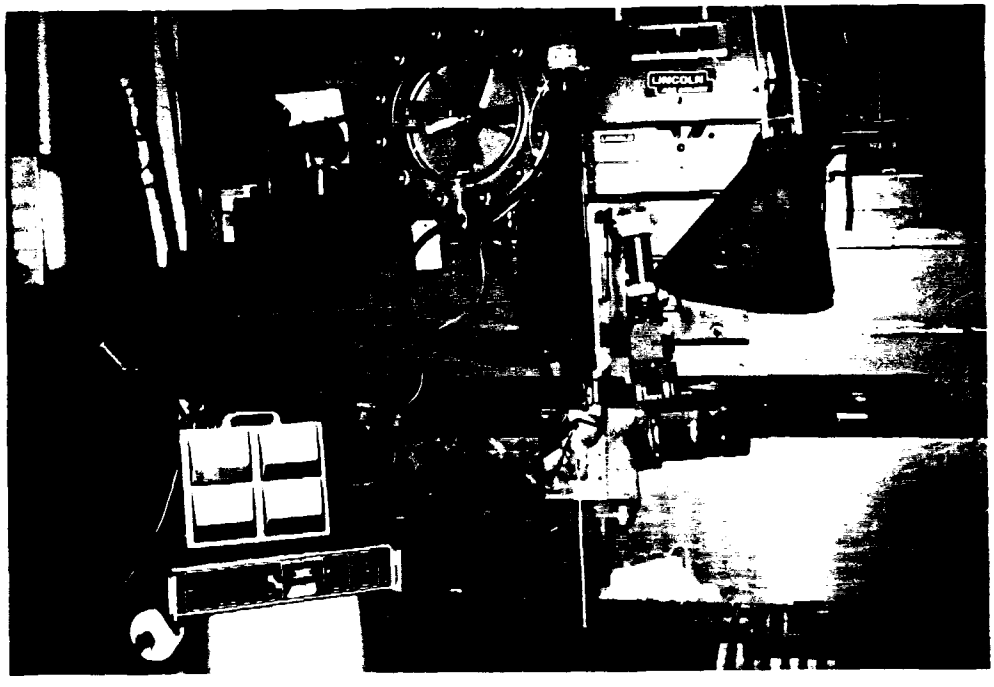

A

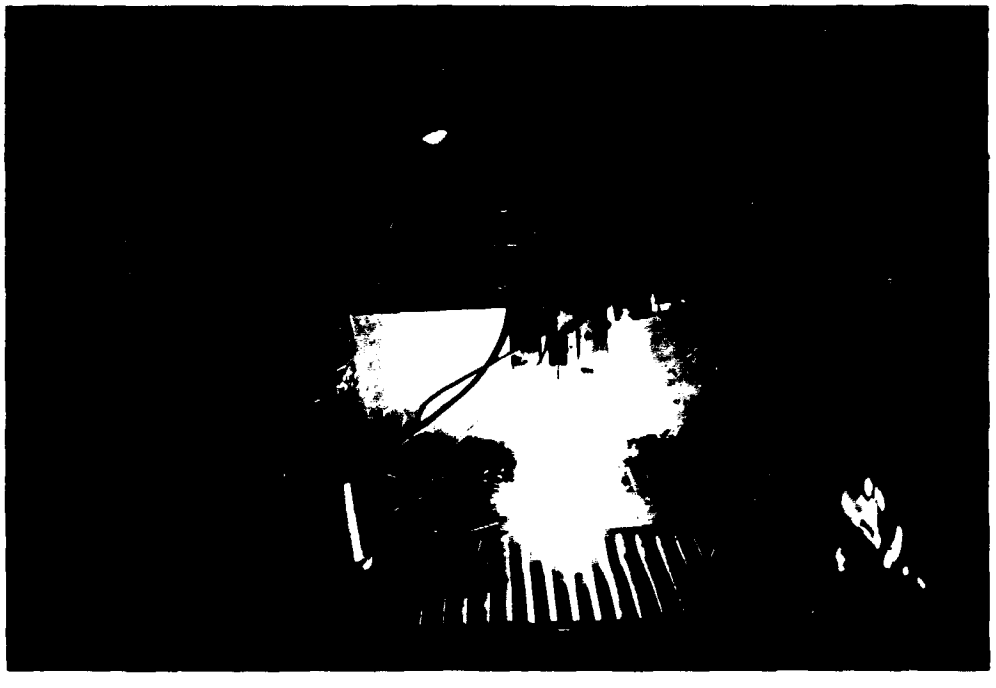

B

Figure 41. Automatic shielded metal arc welding equipment setup.

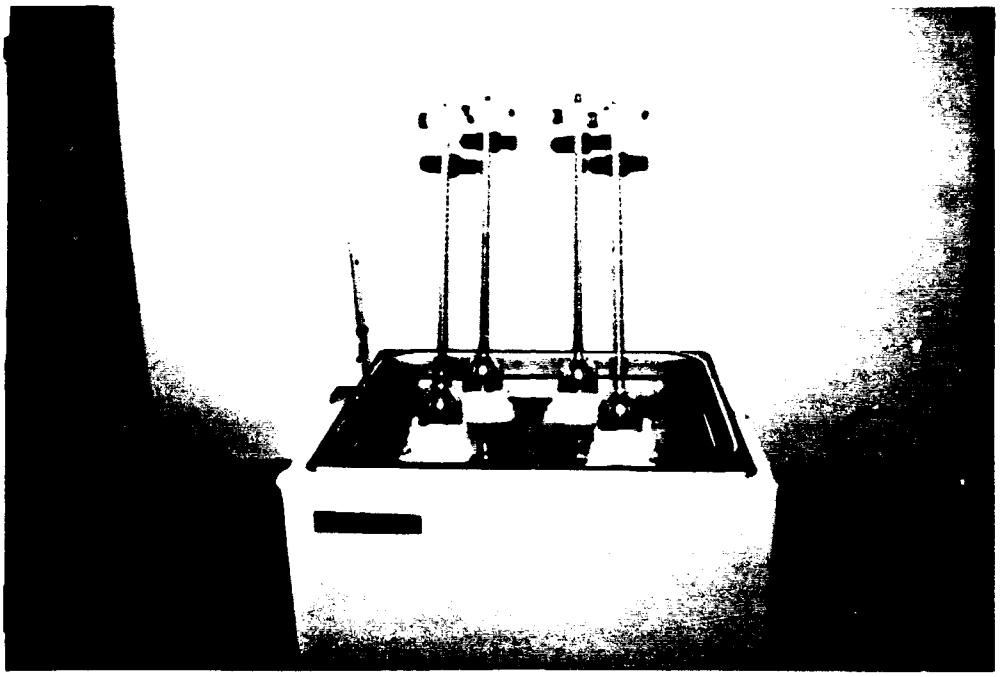

Figure 42. Experimental apparatus for the determination of diffusible hydrogen.

size and shape of the cone is a function of many factors including arc stability, melting temperature of the coating material, and coating thickness. A high arc voltage was observed when a thick coating diameter was used. Since arc voltage is proportional to arc gap, a thick coating in the absence of arc stabilizers will result in a large cone, long arc gap, and high arc voltage.

Coating thickness is typically expressed in terms of $\phi_{coat}/\phi_{electrode}$, a ratio of the coating diameter to electrode diameter. Typically, commercial low hydrogen electrodes have a ratio of $\phi_{coat}/\phi_{electrode}=1.70$. Initially, a ratio of $\phi_{coat}/\phi_{electrode}=1.85$ was used for the CB2 flux composition, and a high voltage (40 volts) resulted. Arc stabilizers such as TiO_2 or Na_2TiO_3 could have been added to lower the welding voltage. However, addition of a strong deoxidizer such as titanium at the present stage of research will not allow any direct correlation between the SA and the SMA welding research (arc stabilizers were not used in the SA welding experiments). Upon reducing the coating-to-electrode diameter ratio to 1.68 and using a mixed sodium and potassium silicate binder, the voltage for the CB2 flux composition was reduced to 30 volts. The composition of flux AA7 also required a relatively high voltage (28 volts) during welding. Both of the compositions CA9 and CB9 were capable of welding with voltages lower than 25 volts without the aid of arc stabilizers. These results are very encouraging since they indicate that a good arc stability can be obtained with the experimental electrodes without significant changes in the flux composition.

The compositions of the as-extruded flux coatings are listed in Table VI. The compositions are slightly different from the compositions specified in the SAW portion of this research because of the adjustments made to the binders to provide an extrudable flux.

Table VI. Actual Composition of the experimental shielded metal arc welding electrode coatings.

Flux ID	$CaCO_3$ (wt.pct.)	CaF_2 (wt.pct.)	SiO_2 (wt.pct.)	Fe (wt.pct.)	K_2SiO_3 (wt.pct.)	Na_2SiO_3 (wt.pct.)
CB2	9.8	19.1	29.4	19.6	11.5	10.6
CB9	9.1	36.4	9.1	18.2	13.6	13.6
CA9	18.8	37.6	9.6	18.8	7.6	7.6
AA7	37.6	28.2	0	18.8	7.7	7.7

II.2.2.2. Electrode Performance

Performance of the electrodes in terms of bead morphology, slag detachability, and spatter are listed in decreasing order as follows: CA9, CB9, AA7, and CB2. Coating CA9 exhibited the best performance, and CB2, the worst. Both fluxes CB2 and AA7 established high welding voltages of 30 V and 28 V, respectively. However, high voltage in these electrodes may be due to the lack of arc stabilizers present in the flux and not related to the protective ability of the slag system. The flux composition CB2 did not produce an adequate slag at high welding currents and voltages relative to the other experimental electrodes. When currents in excess of 110 A were used, the slag became fluid and burned off leaving the weld bead uncovered. The surface quality of weld HCB2 is shown in Figure 43. Electrode AA7 provided superior penetration and had adequate slag coverage even at a heat input approaching 1.5 kJ/mm (38.1 kJ/in.). The high $CaCO_3$ in flux AA7 resulted in more spatter than observed using the other experimental electrodes. However, the appearance of the weld produced using the AA7 electrode resembled an commercial slag because of the absence of SiO_2 in the flux, Figure 44. Electrodes CB9 and CA9 produced superior bead morphology, slag coverage, and slag detachability, Figures 45 and 46. Both electrodes were capable of welding with less than 25 volts. These consumables exhibited good electrode weldability, to the point of being comparable to many commercial electrodes.

II.2.2.3. Weld Metal Chemistry

Four welds were made with a constant heat input of 1.3 to 1.4 kJ/mm and two welds were produced at 1.1 kJ/mm. The compositions of the SMA welds produced are listed in Table VII. Notice that the alloy contents in these welds are lower than those produced in the SA welding experiments (in particular, manganese and chromium are low). This difference occurred because of the lower alloy content of the ER100S-1 electrode relative to the Airco AX-140 electrode used in the submerged arc experiments.

Flux compositions CB9 and CA9 appear to provide the best alloy recovery. These compositions also had the lowest penetration and lowest dilutions, as shown in Table VIII. Lower arc voltages in these two electrodes may also explain the smaller alloy losses to the slag. Because of the shorter arc column, the chemical elements being transferred are not as exposed to the atmosphere. Welds CB2 and AA7 experienced higher losses in manganese and chromium than the CA9 and

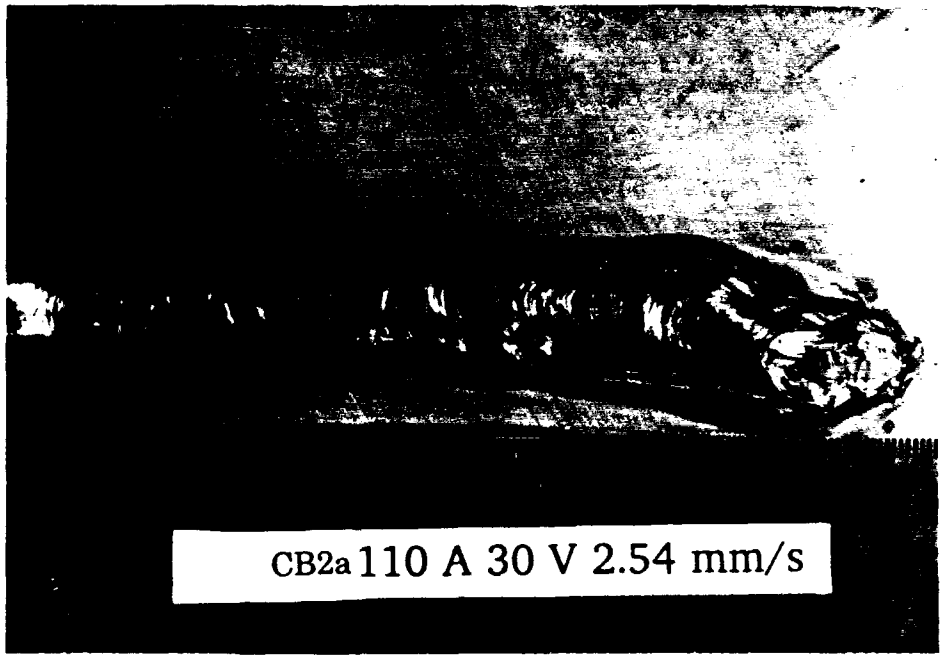

Figure 43. Bead morphology of weld CB2a.

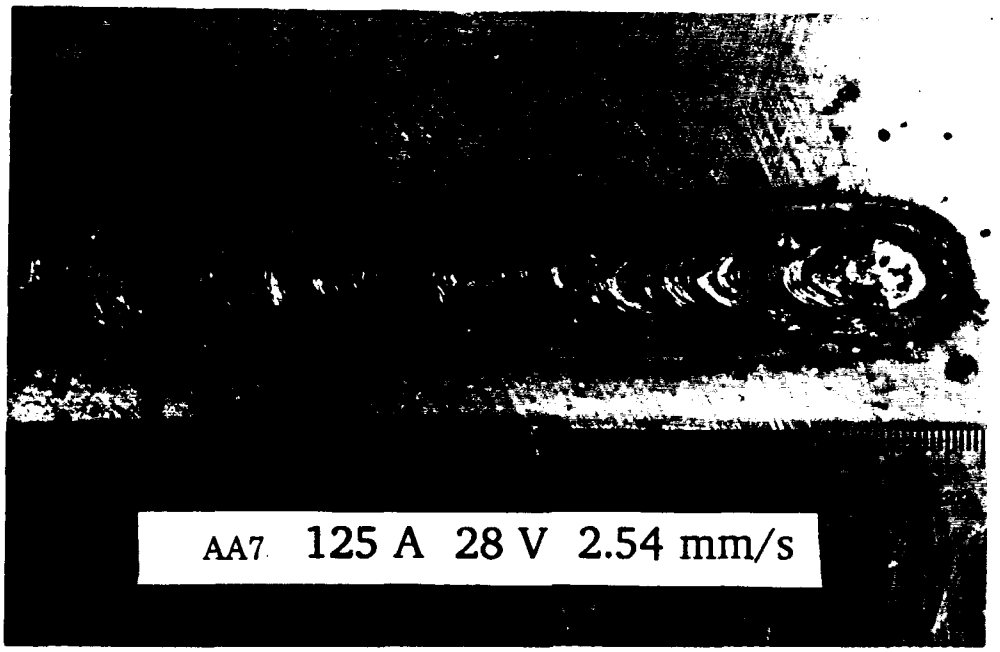

Figure 44. Bead morphology of weld AA7.

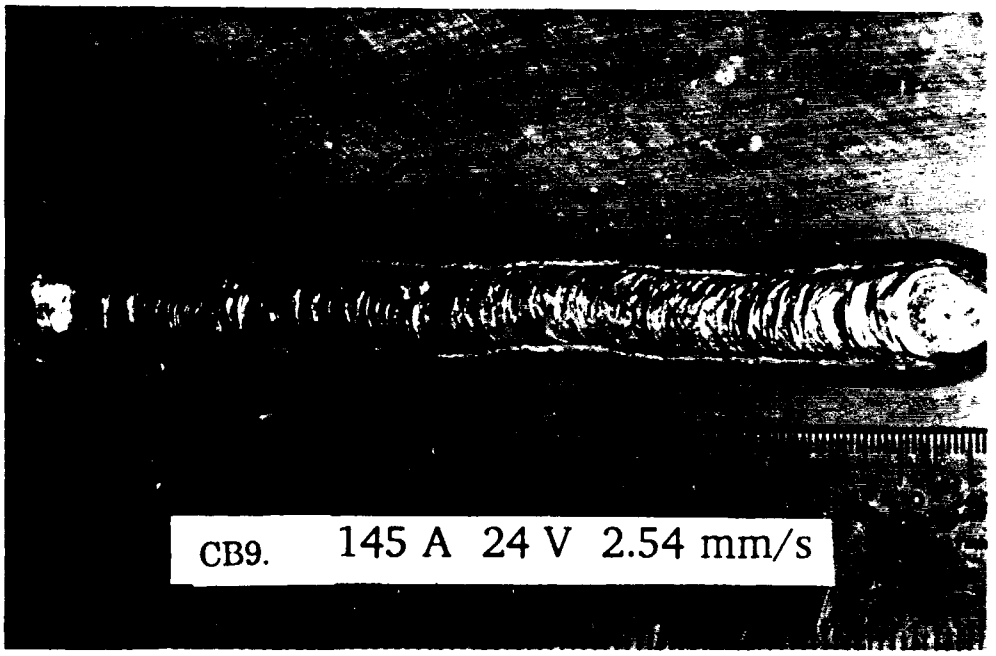

Figure 45. Bead morphology of weld CB9.

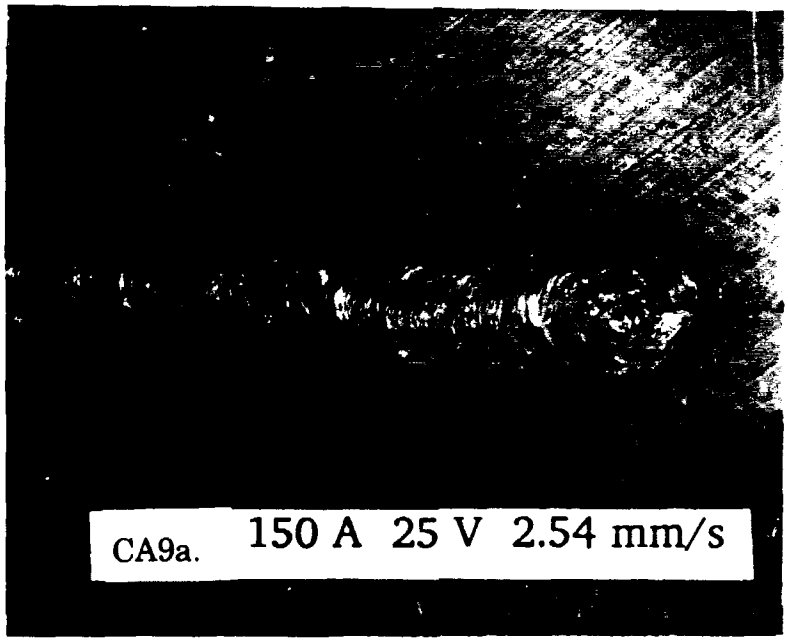

Figure 46. Bead morphology of weld CA9a.

Table VII: Chemical composition (in wt. pct.) of the experimental welds.

Weld ID	C	Mn	Si	Ni	Mo	Cr	Cu	V	Ti	P_{cm}	HI (kJ/mm)
CB2a	0.034	0.41	0.48	2.59	0.52	0.28	0.79	0.002	0.002	0.20	1.33
CB2b	0.027	0.38	0.48	2.46	0.51	0.23	0.65	0.002	0.002	0.18	1.14
CB9	0.023	0.41	0.33	2.29	0.47	0.21	0.53	0.002	0.002	0.16	1.37
CA9a	0.036	0.47	0.47	2.50	0.50	0.25	0.64	0.007	0.003	0.19	1.40
CA9b	0.020	0.45	0.29	2.41	0.49	0.25	0.65	0.006	0.002	0.17	1.13
AA7	0.044	0.53	0.08	2.75	0.52	0.29	0.86	0.003	0.002	0.21	1.40

CB9 fluxes. Based on the calculation of compositional changes in the weld pool, the loss of hardenability elements in AA7 may be attributed to the lack of deoxidizers such as silicon present in the weld pool.

Table VIII. Dilution, bead width and depth of the experimental welds.

Weld ID	Weld Dilution (%)	Bead Width (mm)	Bead Depth (mm)
CB2a	56	14.77	1.9
CB2b	43	13.1	2.9
CB9	41	12.2	1.3
CA9a	41	11.9	2.4
CA9b	44	12.8	1.6
AA7	61	12.7	2.9

Interstitial oxygen analysis, currently in progress, may give further insight into the loss of hardenability elements. Additions such as Fe-Si or Fe-Ti may be necessary to scavenge oxygen and minimize alloying element losses.

Estimates of the ultimate tensile strength of the experimental welds are shown in Table IX. Ultimate tensile strengths of 117-132 ksi were predicted for the experimental welds based on the Brinell hardness data. Yield strengths are expected to vary between 90 and 105 ksi. These strength values are encouraging since they match well the properties of the HSLA-100 base plate used in this in-

vestigation. If a higher strength material is used, the strength of the weld metal is also expected to increase.

Table IX: Hardness and Strength estimates for the experimental welds.

Weld ID	Brinell Hardness	σ_{UTS} (ksi)	σ_y (ksi)
CB2a	254	120	110
CB2b	250	117	107
CB9	252	120	110
CA9a	237	112	102
CA9b	276	132	122
AA7	250	117	107

The lower levels of chromium and manganese compared to the SA welds may explain the lower strengths observed. The lower alloy elements produced using the ER100S-1 core electrode may be experimentally beneficial since the use of this electrode offers the flexibility of increasing the strength of welds by additions to the flux of ferromanganese, ferrochromium or microalloying elements such as titanium, vanadium, and niobium. The specific effect of adding macro- and microalloying elements on the microstructure and mechanical properties is worthy of further investigation. Such additions can be made in a systematic manner so that the resultant changes in the microstructure and mechanical properties can be correlated.

II.2.2.4. Weld Metal Microstructure

Figures 47 to 52 show a mixed microstructure of primary ferrite, AF, FS[A], FS[NA], and MAC. Overall, the microstructure is somewhat coarser than the microstructures obtained during the SA welding research, which seems to agree with the lower alloying element content in the SMA welds. Charpy-V-notch testing is in progress to determine the toughness of these welds.

II 2.2.6. Weld Metal Hydrogen Determination

Diffusible hydrogen tests were conducted on all four SMA welding flux compositions. Very low amounts of hydrogen were collected for electrodes AA7, CB9, and CA9, but CB2 had a slightly higher level. The results of the hydrogen tests are listed in Table X. Diffusible hydrogen levels of less than 3 ml H_2 STP/100 g weld

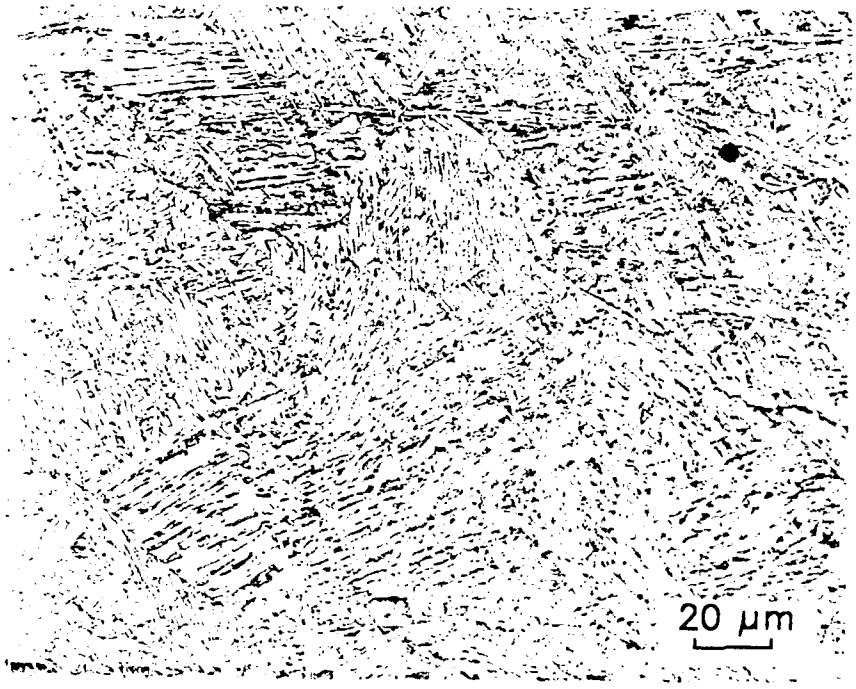

Figure 47. Light micrograph of weld AA7

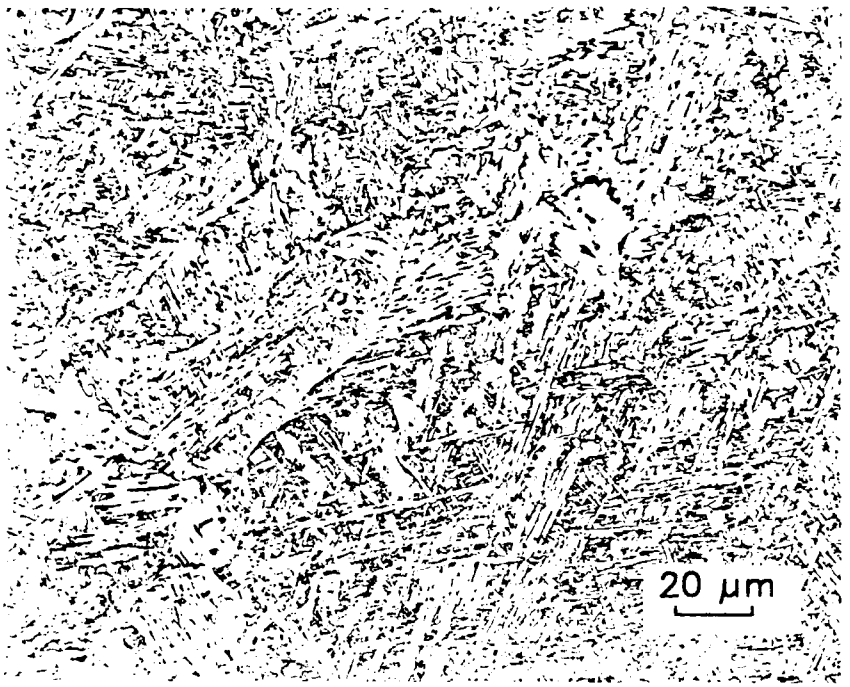

Figure 48. Light micrograph of weld CA9a.

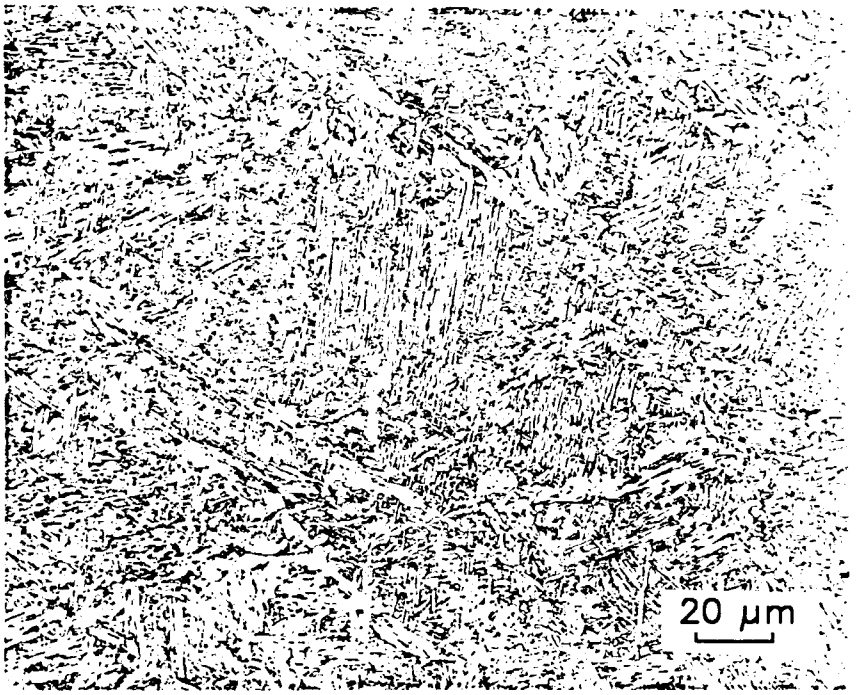

Figure 49. Light micrograph of weld CA9b.

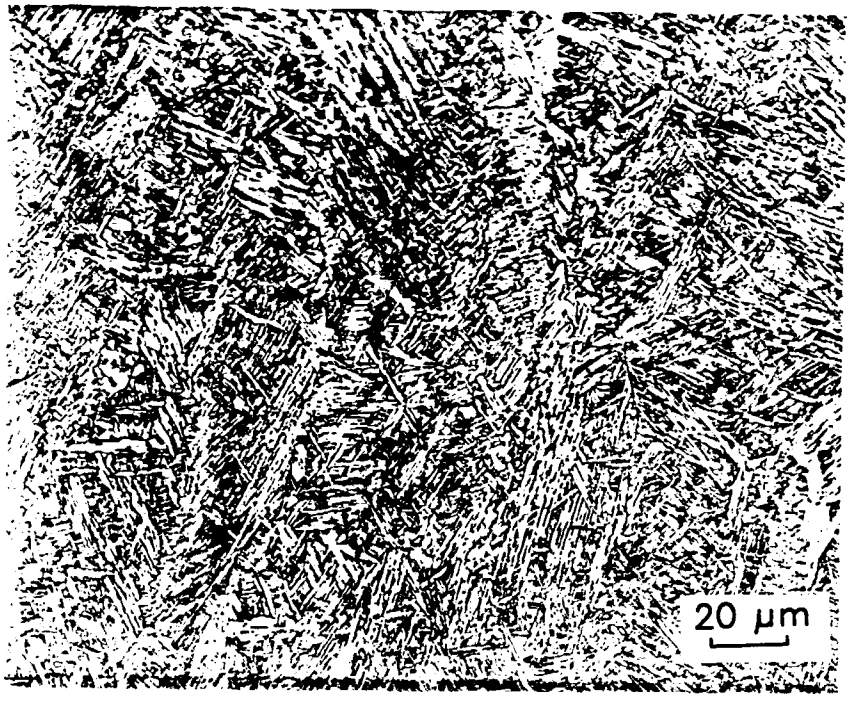

Figure 50. Light micrograph of weld CB2a.

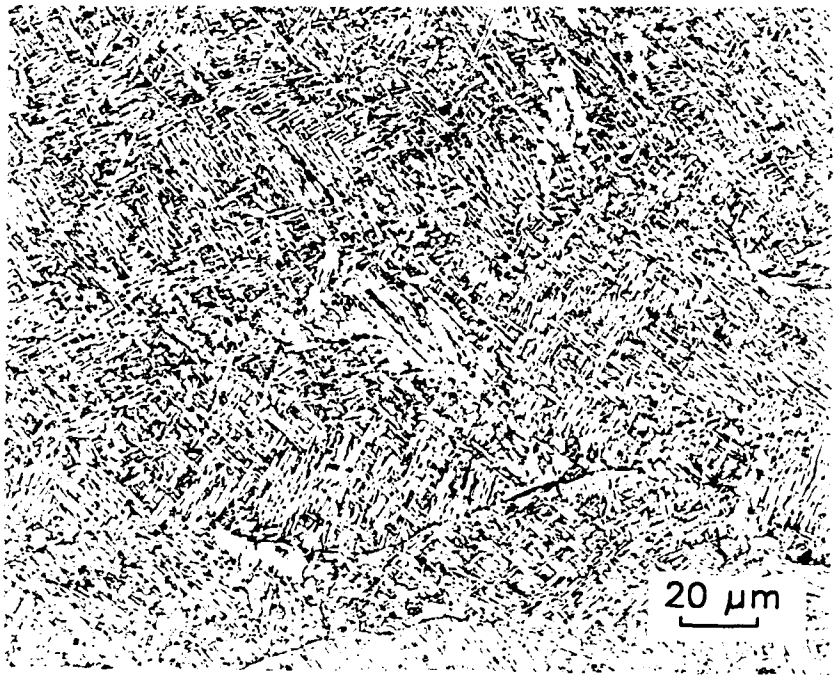

Figure 51. Light micrograph of weld CB2b.

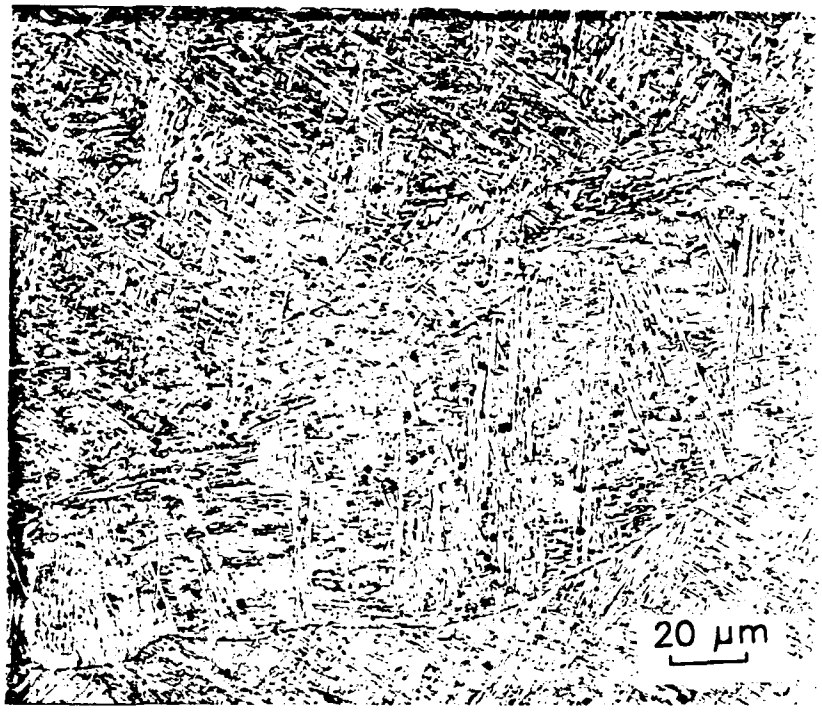

Figure 52. Light micrograph of weld CB9.

metal are considered necessary to prevent hydrogen cracking in high strength steels. These very low levels of diffusible hydrogen produced using the experimental electrodes are very encouraging, since the use of sodium and potassium binder systems are generally thought to produce high diffusible hydrogen volumes. The high levels of diffusible hydrogen observed using flux CB2 may be explained by the low amounts of CaF_2 and $CaCO_3$. Together, CaF_2 and $CaCO_3$ made up only 28.9 wt. pct. of flux CB2. The other compositions consisted of a higher percentage of the two components (CB9 - 45.5 wt. pct, CA9 - 56.4 wt. pct, AA7 - 65.8 wt. pct). When CaF_2 and $CaCO_3$ decompose in the arc column, CO_2 gas and F_2 or SiF_4 gas are generated. An increase in the relative amounts of these gases may lead to a large decrease in the partial pressure of the H_2 gas in the arc column, and a lower hydrogen pickup in the weld metal.

Table X. Weld metal diffusible hydrogen collected over mercury at 45°C for 72 hours.

Weld ID	Diffusible Hydrogen (ml H2/100 g weld metal)
AA7	1.69
CA9	1.80
CB9	1.74
CB2	7.93

A low value of diffusible hydrogen does not necessarily ensure that this particular weld metal is resistant to hydrogen cold cracking. Other tests such as Implant tests, Lehigh tests, and bend tests must be used to more directly evaluate the effect of hydrogen on the cracking sensitivity of this weld metal.

III. Conclusions to Date

1. B_I and B_z are good indicators of the viscosity and melting temperature of welding fluxes, and can be used successfully to describe the morphology of a weld bead.

2. B_I and B_z cannot be used to accurately predict specific chemical properties of the weld metals such as oxygen pickup and alloying element transfer.

3. Similar to low carbon structural steel weld metal microstructures, the final weld metal microstructure of a high strength steel is largely determined by oxygen content.

4. In high strength steel weld metal, as weld metal oxygen content increases, the amount of acicular ferrite decreases while ferrite with second phase aligned increases.

5. Weld metal toughness increases with decreasing oxygen and increasing acicular ferrite.

6. To obtain adequate microstructure (high AF/FS[A] ratio) and Charpy impact toughness, the flux for welding a high strength steel must limit the weld metal oxygen content between 300 to 400 ppm.

7. Using the SA welding results, SMA welding electrodes have been extruded and welded with successfully, producing good quality welds.

8. The experimental SMA welding electrodes produced extremely low diffusible hydrogen contents, less than 2 ml/100g of weld metal.

IV. On-Going Tasks

1. Alloy additions will be made to the SMA welding flux to increase the strength levels and refine the microstructure.

2. Charpy impact specimens will be used to evaluate the toughness of the welds and the success of the alloying additions.

3. Interstitial oxygen, nitrogen, carbon, and sulfur analysis will be conducted.

4. Quantitative metallography will be performed to evaluate the percentage of the different microstructural components observed.

5. Modifications of the flux coating will be made to enhance the performance of the experimental electrodes in out-of-position welding.

6. A slag analysis will be conducted to define a relationship between flux composition and weld metal alloy content.

7. Multiple-pass welding will be used to generate full size Charpy specimens and sub-size tensile specimens. This will allow impact data from this study to be related to other studies.

8. Additional funding is requested to continue this unique research. A more fundamental understanding of the relationships between SA and SMA welding fluxes and a basic understanding concerning the role which individual slag ingredients play in protecting the weld pool are badly needed if consumables development for high strength steels are ever to escape the regime of "cut and try" empiricism.

V. Acknowledgment

The authors gratefully acknowledgment the research support of the Office of Naval Research and David Taylor Research Center.

VI. References

1. G. R. Edwards and S. Liu. "Shielded Metal Arc Welding Consumables for an Advanced High Strength Steel", CSM Report MT-CWR-091-006, 1991.

2. IIW. "Guide to the Light Microscope Examination of Ferritic Steel Weld Metals", IIW DOC IX-1533-88, 1988.

3. J. Zeke. "Recommendation for Expressing the Flux Basicity by means of the Oxygen Anion Ionic Fraction", IIW DOC XII-803-83, 1983.

4. B. Chew. "Moisture Loss and Regain by Some Basic Flux Covered Electrodes", Welding Journal 55(8):629, 1976.

5. AWS A5 Committee. "Specifications for Covered Carbon Steel Arc Welding Electrodes", AWS A5.1.81, Section 13.12, 1981.

6. AWS. "Standard Methods for Determination of the Diffusible Hydrogen of Martensitic, Bainitic, and Ferritic Steel Weld Metal produced by Arc Welding", AWS A4.3.86, 1986.

VII. Research Personnel

Dr. Glen R. Edwards - Co-Principal Investigator
Dr. Stephen Liu - Co-Principal Investigator
Mr. G. L. Fredrickson - M.S. Candidate (Conclusion: 04/1992)
Mr. M. Q. Johnson - M.S. Candidate

VIII. Related Publications and Presentations

1) G. L. Fredrickson, S. Liu, and G. R. Edwards. "An Investigation of SMAW Consumables Development for HSLA-130 Steel", presented at the 1991 AWS Welding Conference, Detroit, Michigan.

2) G. L. Fredrickson, M. Q. Johnson, S., Liu, and G. R. Edwards. "An Investigation of SMAW Consumables Development for HSLA-130 Steel", to be presented at the 1992 AWS Welding Conference in Chicago, Illinois.

3) M. Q. Johnson, G. L. Fredrickson, S. Liu, and G. R. Edwards. "Consumable Development for Advanced High Strength Steels", to be presented at the 1992 International Conference on Trends in Welding Research, Gatlinburg, Tennessee.

List of Figures